Geomorphology 421 (2023) 108527

Contents lists available at ScienceDirect

Geomorphology

journal homepage: www.journals.elsevier.com/geomorphology

# Geology, geomorphology and geochronology of the coseismic? Emad Deh rock avalanche associated with a growing anticline and a rising salt diapir, Zagros Mountains, Iran

Francisco Gutiérrez [a,*], Hosein Deirnik [b], Mehdi Zarei [b], Alicia Medialdea [c]

[a] University of Zaragoza, Pedro Cerbuna 12, 50009 Zaragoza, Spain
[b] Shiraz University, Shiraz, Iran
[c] Centro Nacional de Investigación sobre la Evolución Humana, Burgos, Spain

ARTICLE INFO

*Keywords:*
Earthquake-induced landslide
Long-runout landslide
Hummock
Growing fold
Active diapir
Flexural-slip faulting

ABSTRACT

This work documents for the first time the prehistoric, but morphologically pristine, Emad Deh rock avalanche of the Zagros Mountains. The ca. 420 $Mm^3$ rock avalanche was initiated as a rockslide on a dip slope affecting a weak unit of marls with interbedded limestones overlain by a thick and competent limestone formation. The slope is located on the northern limb of the growing Gavbast Anticline and at the edge of the inflating Gavbast Dome, related to a buried salt diapir of Hormuz salt. The unconfined rock avalanche deposits, covering 32 $km^2$, were accumulated on coalescing alluvial fans and a floodplain environment. The depositional lobe shows sectors with distinctive morphological features attributable to the variable flow-depositional behavior of the debris stream, controlled by the nature of the substrate: (1) proximal continuous breccia flanked by levees; (2) intermediate depression; and (3) flat-topped polygonal hills and conical hills. A morphometric and spatial distribution analysis has been performed with the 550 conical hills (hummocks) mapped in the distal sector. The rock avalanche, with 914 m of maximal height drop (H) and 9280 m of runout (L), displays an extraordinarily high mobility (H/L index of 0.09), that can be attributed to the combined effect of dynamic rock fragmentation and basal lubrication by the soft substrate in the floodplain. Relief rejuvenation and slope over-steepening related to the growth of the anticline and the inflation of the Gavbast Dome are considered the main long-term preparatory factors that shifted the slope to a state of marginal stability. The slope failure was likely triggered by a large $M \geq 6.5$–7 earthquake at ca. 5.4 ka, as indicated by OSL ages obtained from folded alluvium situated just beneath the rock avalanche deposit. The source of the earthquake was probably a blind reverse fault situated beneath the asymmetric Gavbast Anticline, as support the structural and geomorphic features of the fold. The identification and dating of large coseismic landslides in the Zagros Mountains, where large earthquakes are rarely accompanied by primary surface ruptures, could help to improve both landslide and seismic hazard assessments.

## 1. Introduction

Prehistoric large rapid landslides, and notably rock avalanches, show a relatively high spatial frequency in the Zagros Mountain Belt, related to the ongoing collision between the Arabian and Eurasian plates. Here, slope instability is instigated by a number of static and dynamic factors, including the presence of anticlinal ridges with steep dip slopes on competent limestones underlain by weak marls, relief rejuvenation related to active deformation (i.e., slope and dip over-steepening), and frequent large earthquakes (Ghazipour and Simpson, 2017; Goorabi, 2020). However, these large catastrophic landslides (>$10^6$ $m^3$, >30 m/s) with high damaging capability and major impact on landscape development have received very limited attention compared with other less densely populated active orogens worldwide (e.g., Hewitt et al., 2008; Strom et al., 2019). The perception of the potential societal and economic impacts of such catastrophic failures that can suddenly bury areas tens or even hundreds of square kilometers is almost lacking, probably due to the fact that they have not been responsible for any major disaster in historical times. A similar situation occurred in other seismically active mountain regions until the occurrence of events involving large numbers of fatalities, such as the coseismic 1962 and 1979 Huascarán avalanches of Perú (ca. 7000 fatalities, Plafker and

* Corresponding author.
*E-mail addresses:* fgutier@unizar.es (F. Gutiérrez), zareim@shirazu.ac.ir (M. Zarei), alicia.medialdea@cenieh.es (A. Medialdea).

https://doi.org/10.1016/j.geomorph.2022.108527
Received 27 June 2022; Received in revised form 25 October 2022; Accepted 5 November 2022
Available online 18 November 2022

Ericksen, 1978; Evans et al., 2009), or recent avalanches occurred in Pakistan (2005, M7.6 Kashmir earthquake) and the Philippines, each killing >1000 people (Harp and Crone, 2006; Lagmay et al., 2006). The most remarkable example in the Zagros Mountains is the gigantic Seymareh rock avalanche (44 $Gm^3$; 220 $km^2$), considered the largest subaerial rock slope failure worldwide (Roberts, 2008; Roberts and Evans, 2013; Shoaei, 2014; Delchiaro et al., 2019, 2022; Rouhi et al., 2022). This landslide was initiated by the detachment along multiple bedding planes of a rock slab comprising a weak unit of marls with limestone interbeds capped by thick and resistant limestone. The rock avalanche created a scar 15.5 km wide and 7 km long, plus three large landslide-dammed lakes (Roberts and Evans, 2013; Sharafi et al., 2019), involving major and enormous instantaneous geomorphic work and long-persistent landscape changes (Delchiaro et al., 2019, 2022). According to Roberts (2008), the energy released by the single-event Seymareh rock avalanche ($10^{18}$ J) is comparable to that of the 2005, M9 Great Sumatra earthquake (Lay et al., 2005). The coseismic nature of some of these rock slope failures, and hence their condition of secondary paleoseismic evidence, can be supported by various types of back analyses (Rajabi et al., 2011; Jibson, 2012), as it has been illustrated for the Seymareh rock avalanche (Fomenko et al., 2021).

The Zagros orogen is one of the most seismically active and more rapidly deforming mountain belts in the world. However, large damaging earthquakes are very rarely accompanied by primary surface ruptures. These large events are mostly sourced from blind high-angle reverse faults, which propagation is impeded by the thick Hormuz salt or other detachments within the sedimentary cover (Jackson, 1980; Berberian, 1995; Talebian and Jackson, 2004). The only known historical reverse fault earthquake with associated primary surface ruptures was the Furg, 6 November 1990, $M_w$ 6.5 event on the High Zagros Fault (Walker et al., 2005). The hidden condition of the seismogenic faults significantly restricts the possibilities of integrating fault sources and paleoseismic data in seismic hazard analyses, with detrimental impact on their reliability (Berberian, 1995). This limitation could be partially overcome by identifying and dating secondary paleoseismic evidence such as coseismic landslides (Jibson, 2009) or secondary surface ruptures (e.g., flexural-slip faults; Walker et al., 2015), which could be used to expand the paleoearthquake catalog and infer the main seismogenic sources.

This work documents for the first time the prehistoric and likely coseismic Emad Deh rock avalanche of the Fars Arc (Zagros Mountains), developed on the limb of a growing anticline and associated with an inflating dome related to a buried salt diapir. The main objectives of this multidisciplinary study include: (1) Describing the geological, seismotectonic and tectonic-geomorphology setting of the Fars Arc, providing the basis for understanding the main factors that control the development of large rapid landslides in the region, including the Emad Deh rock avalanche. (2) Characterizing the Emad Deh rock avalanche and inferring its flow-depositional behavior considering the variable substrate and morphology. (3) Analyzing the morphometric features and spatial distribution patterns of the remarkable field of hummocks deposited in its distal sector. (4) Constraining the timing of the rock avalanche by OSL-dating of the deformed alluvium underlying the rock avalanche deposit. (5) Analyzing the main controlling factors and documenting the impact of fold growth and active diapirism on the development of large landslides (Emad Deh rock avalanche and other large landslides). (6) Inferring on the basis of structural and tectonic-geomorphology criteria the most probable source for the putative large earthquake responsible for the triggering of the Emad Deh rock avalanche.

## 2. Setting

### 2.1. General geological setting

The NW-SE-oriented Zagros Fold-and-Thrust Belt, located in the middle part of the Alpine-Himalayan orogenic system, extends along 1800 km between the Taurus Mountains in Turkey and the Makran Accretionary Prism east of the Hormuz Strait, covering around 400,000 $km^2$ (Fig. 1). This fold and thrust belt lies on the northeastern margin of the Arabian Plate and results from the closure of the Neo-Tethys ocean and the ongoing Cenozoic collision between the Arabian and Eurasian plates. A total shortening of around 50–80 km has been estimated by various authors (Blanc et al., 2003; McQuarrie, 2004; Molinaro et al., 2005; Sherkati et al., 2005, 2006; Mouthereau et al., 2007). The Zagros Fold-and-Thrust Belt is divided into two main longitudinal structural zones (Fig. 1): the High Zagros on the NE and the Simply Folded Belt on the SW. The 70–90 km wide High Zagros (or Imbricated Belt) is bounded by the High Zagros Fault on the SW and the Main Zagros Reverse Fault on the NE, which is widely regarded as the suture between the Arabian and Eurasian plates (Stöklin, 1968). The 100–250 km wide Simply Folded Belt is situated between the High Zagros Fault and the vaguely-defined Zagros Deformation Front. The latter corresponds to the NE edge of the current foreland basin associated with the Persian Gulf and the Mesopotamian Plain. The Simply Folded Belt comprises three domains with different sedimentary and tectonic features bounded by major oblique N-S and *E*-W trending fault zones, from NW to SE (Motiei, 1993) (Fig. 1): (1) the Lurestan Arc north of the Balarud Fault; (2) the Dezful Embayment; and (3) the Fars Arc east of the Kazerun Fault, where the Emad Deh rock avalanche is located. The structural variability observed across these domains, expressed as two salients and a re-entrant, is mainly attributed to different rheological profiles and main detachment horizons: (1) Mesozoic shales and evaporites 2–3 km thick in the Lurestan Arc; (2) the 1.5 km thick Miocene Gachsaran evaporites in the Dezful Embayment; and (3) the highly mobile 1–1.5 km thick Neoproterozoic-Cambrian Hormuz salt in the Fars Arc (Sepehr and Cosgrove, 2004).

Since Neoproterozoic times, the region was dominated by sedimentation until the Cenozoic collision between the Arabian and the Eurasian plates, leading to the building up of the Zagros Mountain belt. This orogenic phase is essentially recorded by a regressive succession overlying the laterally extensive Oligocene-early Miocene Asmari Limestone, including the Fars Group (early Miocene-Pliocene) and the continental coarse detrital sediments of the Bakhtyari Formation (Plio-Quaternary) (Motiei, 1993). The Fars Group comprises the marine Gascharan evaporites and the contemporaneous Razak Formation to the NE, the shallow marine Mishan marls, and the marls and sandstones of the Agha Jari Formation deposited in transitional environments. The synorogenic clastics (molasse) of the Bakhtyari Formation lie on a time transgressive angular unconformity that can cut across multiple formations and is considered to record the most vigorous phase of folding and relief creation in each sector of the Zagros. The SW-propagation of the Zagros Deformation Front implies a progressively younger age towards the current foreland for the (Hessami et al., 2001): (1) onset of the contractional structures; (2) the synorogenic sedimentation (e.g., the time-transgressive Bakhtyari Formation; Homke et al., 2004; Fakhari et al., 2008; Khadivi et al., 2010; Vergés et al., 2019); and (3) the initiation of the present-day tectonic landscape, dominated by landslide-prone anticlinal ridges and synclinal valleys.

### 2.2. The Fars Arc of the Simply Folded Belt

The Fars Arc of the Simply Folded Belt is bounded by the Kazerun and Borazjan right-lateral fault systems to the west and the Oman Line (or syntaxis) to the east (Fig. 1). This structural domain is characterized by folds with an overall arcuate arrangement, changing towards the east from the typical NW-SE Zagros trend to an ENE-WSW orientation, roughly perpendicular to the direction of plate convergence. The folds are punctured by numerous emergent and buried salt diapirs of the Hormuz Salt, with an estimated original thickness of around 1–1.5 km (Kent, 1979; Talbot and Alavi, 1996) (Fig. 2). Jahani et al. (2017) propose that the location of the salt structures is guided by basement faults

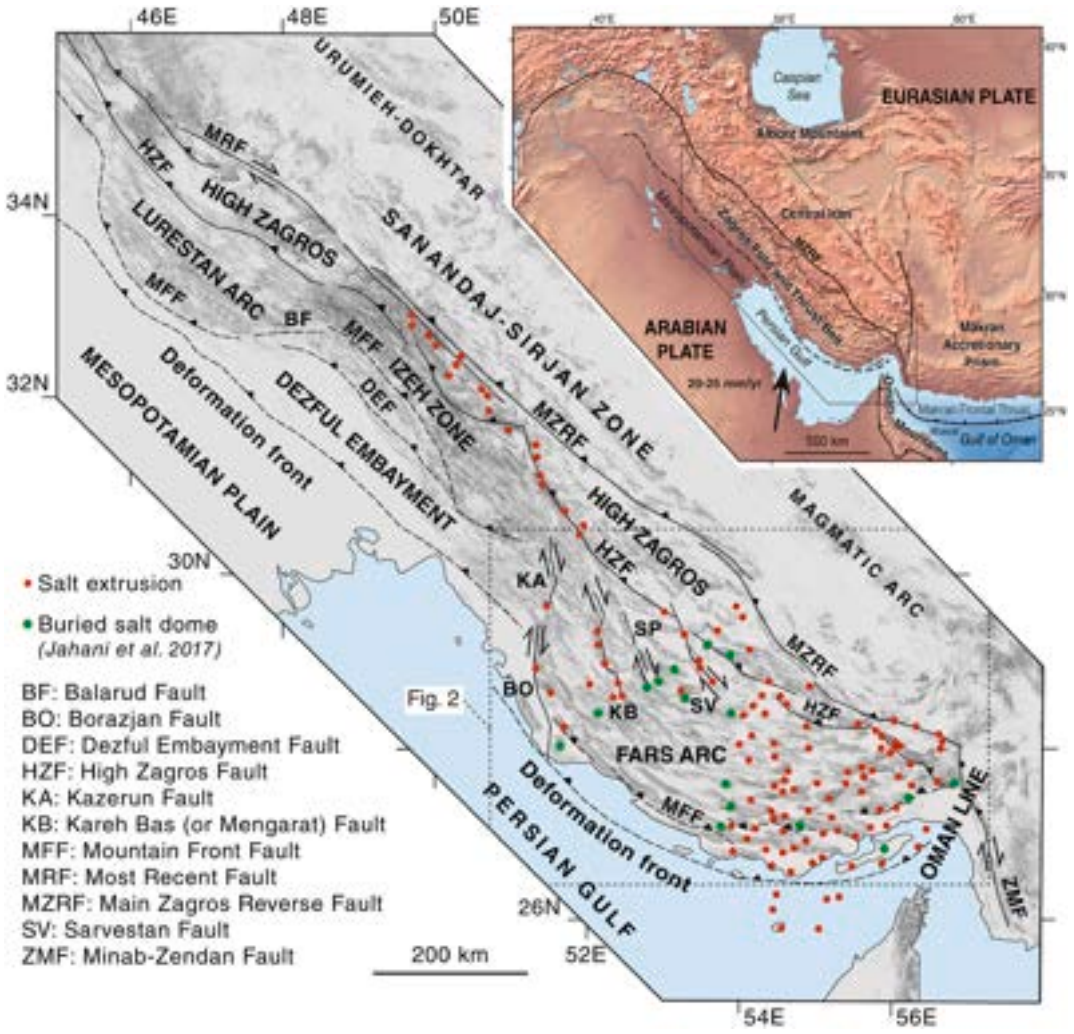


**Fig. 1.** Geotectonic setting of the Zagros Fold-and-Thrust Belt, related to the ongoing collision between the Arabian and Eurasian plates, and sketch of the Zagros orogen showing the structural zones, the main faults and the distribution of salt extrusions and buried salt domes.

that controlled zones with greater thickness of Hormuz salt. The westernmost salt extrusions in the Simply Folded Belt occur associated with the strike-slip faults that define the western margin of the Fars Arc, suggesting that those structures are inherited from basin-bounding faults during Hormuz sedimentation (Sepehr and Cosgrove, 2004) (Fig. 2).

The structural style and thus the tectonic geomorphology in the Fars Arc are largely controlled by the deep Hormuz salt and the related salt diapirs. The Hormuz salt, situated at a depth of 11–15 km (Fig. 2), acts as a major decollement that largely decouples the structure of the Phanerozoic cover, dominated by detachment folds, from the basement, in which shortening is chiefly accommodated by blind reverse faults (Jahani et al., 2009). The greater advance of the deformation in the Fars Arc and the lower taper angle of the orogenic wedge (1° versus 2° in other sectors) are attributed to low basal friction along the Hormuz salt detachment (Talbot and Alavi, 1996; McQuarrie, 2004; Molinaro et al., 2005; Macedo and Marshak, 1999). A significant part of the salt diapirs in the Zagros were initiated in pre-orogenic times, with the Hormuz salt penetrating into an essentially flat-lying overburden, and they have experienced rejuvenation during the Cenozoic collision (Harrison, 1930; Kent, 1979; Jahani et al., 2007, 2009 and references therein). Evidence of upward salt flow in emergent or buried diapirs during pre-orogenic times is recorded by: (1) Hormuz-derived debris in cover sediments deposited by salt sheets in the surroundings of the salt extrusions; (2) thickness and facies variations, hiatuses and growth strata in cover sediments associated with the diapirs. The detachment folds in the supra-salt Phanerozoic cover of the Fars Arc display the following features (Jahani et al., 2009): (1) general upright and symmetric geometry; (2) high half-wavelength/axial length ratio related to the large thickness of the cover (11–15 km), with influence on the dip of the strata; (3) sharp inflections in the anticline axes associated with diapirs; (4) local constrictions in the anticlines linked to salt extrusions; and (5) dome morphostructures superimposed on the anticlines related to buried salt diapirs with enhanced relief and slope gradients, as occurs in the anticlinal ridge that sourced the Emad Deh rock avalanche (Figs. 2 and 3). It is interpreted that the weak salt diapirs penetrating into the Phanerozoic cover before the onset of the collisional folding acted as strain localizers and enhancers, controlling changes in the propagation direction of growing anticlines and locally amplifying the shortening by the squeezing of salt diapirs (Letouzey and Sherkati, 2004; Callot et al., 2007; Jahani et al., 2007, 2009).

The shortening in the basement is mainly accommodated by blind, high-angle NE- to N-dipping reverse faults, probably inherited from normal faults developed during the Permo-Triassic rifting, which are experiencing positive inversion in the current collisional context (Berberian, 1995; Talebian and Jackson, 2004). In the western sector of the Fars Arc, oblique plate convergence and the differential shortening between the Dezful Embayment and the Fars Arc is accommodated by dextral displacement along outcropping N-S strike-slip faults with associated salt extrusions at releasing step overs (Talbot and Alavi,

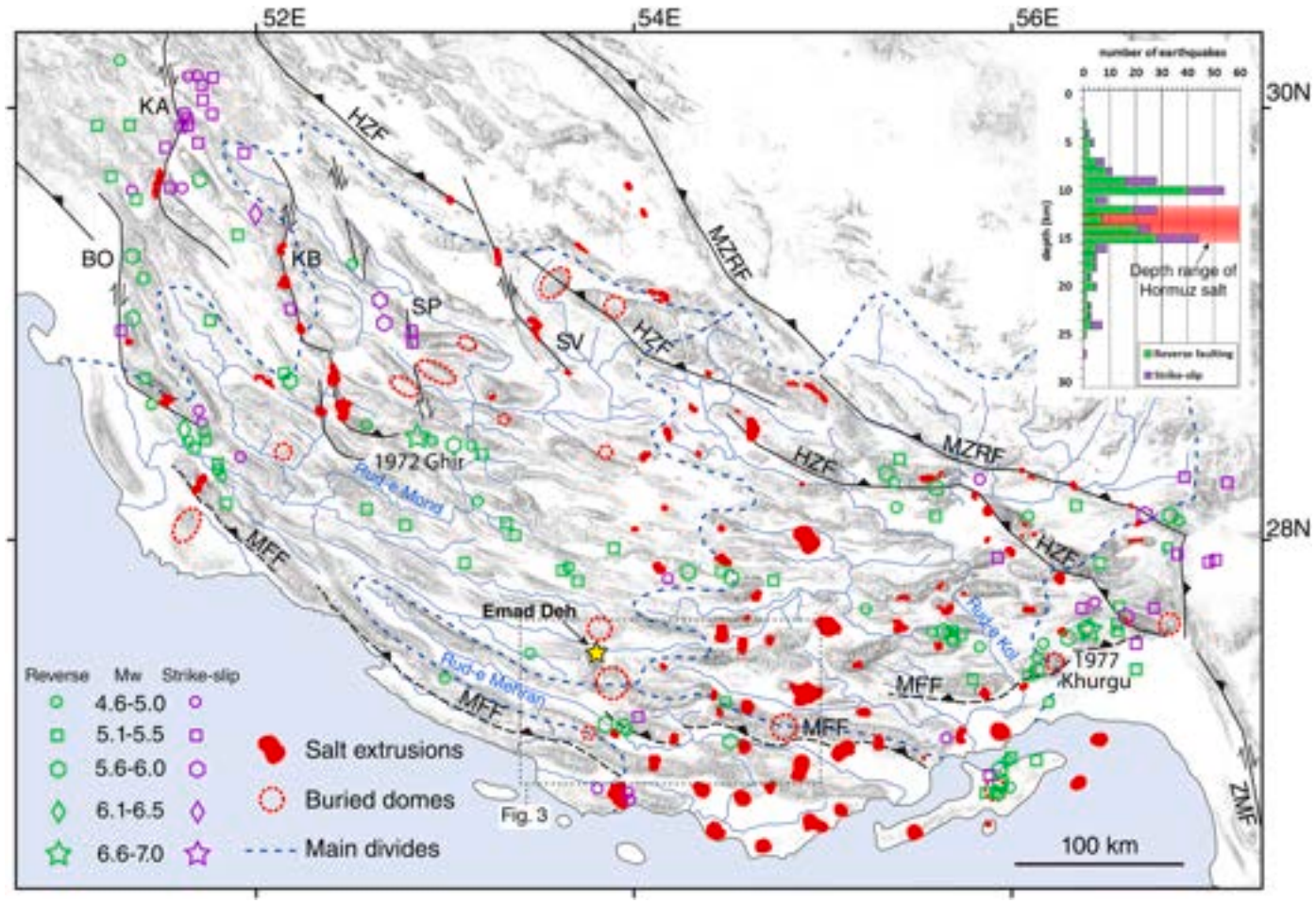


**Fig. 2.** Map of the Fars Arc of the Simply Folded Belt showing the epicenters from the relocated earthquake catalog (1962 to 2018;267 events, error < 5 km) of Karasözen et al. (2019), differentiated by the dominant focal mechanism and $M_w$ intervals. Inset shows the depth distribution of calibrated focal depths for the different faulting styles (Karasözen et al., 2019) and the depth range of Hormuz salt (ca. 12–15 km) inferred by Jahani et al. (2009) on the basis of seismic profiles. The salt extrusions and buried domes indicated by Jahani et al. (2017) are depicted, as well as the main watershed divides and drainage network. The location of the Emad Deh rock avalanche is indicated with a yellow star. (For interpretation of the references to colour in this figure legend, the reader is referred to the web version of this article.)

1996; Walpersdorf et al., 2006; Tavakoli et al., 2008; Authemayou et al., 2009; Jahani et al., 2017) (Fig. 2). In the eastern flank of the Fars Arc associated with the Oman syntaxis, the detachment folds developed in the cover are locally cross cut by oblique out-of-sequence reverse faults, presumably rooted in the basement (Leturmy et al., 2010; Molinaro et al., 2005). According to Berberian (1995), the most important basement reverse fault in the Fars Arc is the Mountain Front Fault, which has a kilometer-scale throw and marks the southwestern limit of exposure of the Asmari Limestone (Fig. 2). The approximate trace of this blind fault was inferred from: (1) asymmetric anticlines in the hanging wall, with steeper southern limbs; (2) significant elevation changes across the anticlinal ridges; (3) evidence of deformation in Quaternary landforms and deposits; and (4) concentration of moderate- and large-sized earthquakes. Berberian (1995) suggests that this is a discontinuous and segmented fault with gaps and step overs that restrict the lateral extent of the seismogenic ruptures and the associated earthquake magnitudes. He inferred a WNW-ESE oriented segment of the Mountain Front Fault along the southern edge of the symmetric Gezeh Anticline, situated just south of the clearly asymmetric Gavbast anticlinal ridge, where the source of the Emad Deh rock avalanche is located (Figs. 2 and 3).

### 2.3. Seismotectonics

According to GPS data, the Arabian and Eurasian plates are converging with a general N-S direction at a rate of 20–25 mm/yr, of which around one third is accommodated within the Zagros Fold-and-Thrust Belt (Vernant et al., 2004) (Fig. 1). Along most of the NW-SE oriented orogen, the oblique N-S convergence is partially accommodated by right lateral displacement, whereas in the central and eastern sector of the Fars Arc the strike-normal displacement results in pure shortening (Walpersdorf et al., 2006; Tavakoli et al., 2008). Seismogenic faulting in the Zagros is strongly influenced by the presence of thick evaporitic detachments. The following major units with contrasting rheology are differentiated in the Fars Arc, from base to top (e.g., O'Brien, 1957; Molinaro et al., 2005): (1) the "rigid basement" of the Arabian metamorphic shield; (2) the "lower mobile group", corresponding to the Hormuz salt, with highly variable thickness largely related to the mobilization of the salt towards the anticlines and salt diapirs; (3) the "competent group", formed by a succession 4–10 km thick dominated by mechanically resistant carbonates up to the top of the Asmari Formation; (4) the "upper mobile group" represented by evaporites of the Gachsaran Formation; and (5) the "incompetent group" including the Mishan and Agha Jari formations. The mechanically weak mobile and incompetent groups tend to restrict the propagation of faults and prevent the formation of coseismic surface ruptures (Berberian,

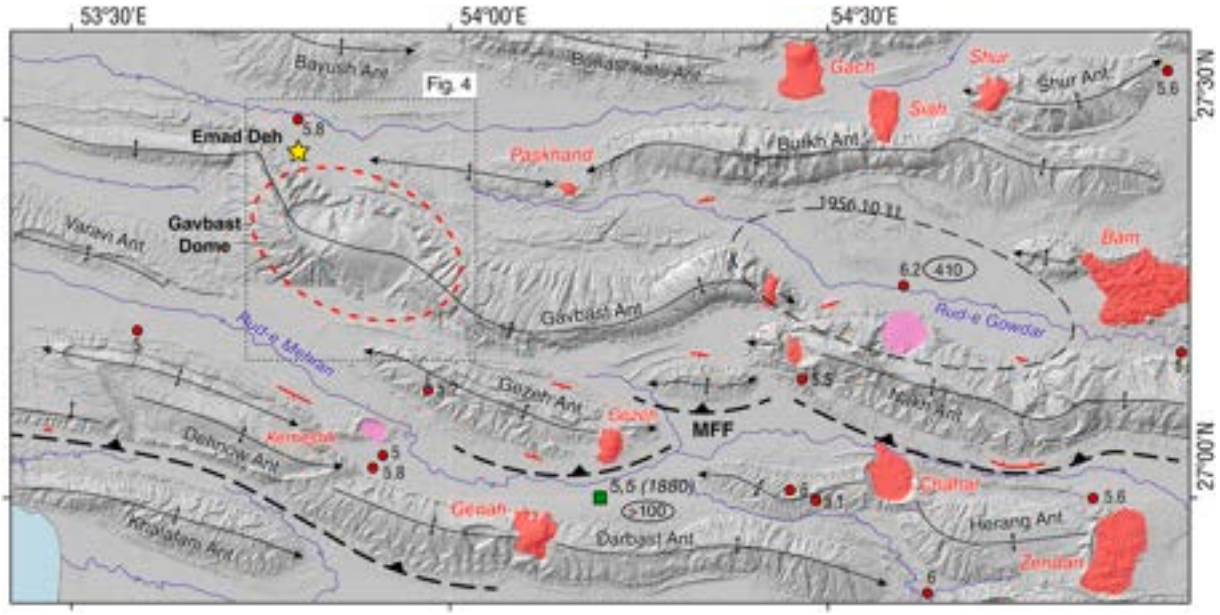


**Fig. 3.** Hillshade showing the distribution of anticlinal ridges, salt extrusions (red) and diapiric craters (pink; vanished salt extrusions) in the vicinity of the Emad Deh rock avalanche (yellow asterisk). The approximate extent of the Gavbast Dome related to a buried salt stock is shown with a red dashed ellipse. The N-dipping Mountain Front Fault (MFF; blind basement reverse fault) inferred by Berberian (1995) is indicated with a dashed trace. Red lines with hachures indicate areas with alluvial fans offset by Quaternary flexural-slip faults related to active folding. Epicenters from the historical catalog of Berberian (2014) (green squares, estimated $M_s$ magnitude) and the instrumentally recorded events with $M_s \geq 5$ (red circles) from Berberian's catalog (1900–2005) and that of the Iranian Seismological Center (2006–2022). Number of people killed in the 1880 Jonah (or Jenah) and 1956 Gowdeh earthquakes indicated within an ellipse. The meizoseismal area of the latter event from Berberian (1995) is indicated with a dashed line. Hillshade generated with TanDEM-X DEMs from the German Aerospace Center. (For interpretation of the references to colour in this figure legend, the reader is referred to the web version of this article.)

1995; Nissen et al., 2011), limiting the use of paleoseismic methods (e.g. trenching across faults) for seismic hazard analyses.

Traditionally, seismicity in the Zagros Fold-and-Thrust Belt has been mainly attributed to blind, high-angle, reverse basement faults, and locally right-lateral wrench faults (e.g., western Fars Arc) (Jackson, 1980; Berberian, 1995; Talebian and Jackson, 2004). Recent data on locally- and teleseismically-recorded earthquakes, and rupture-depth derived from DInSAR analyses (e.g., Lohman and Simons, 2005; Roustaei et al., 2010; Barnhart et al., 2013) reveal that moderate-sized earthquakes ($M_w$ 5–6) also occur within the "competent group" of the cover above the Hormuz salt (Nissen et al., 2011 and references therein). Nissen et al. (2011), based on the distribution of centroid depths, differentiate two main types of reverse fault earthquakes: (1) moderate-sized events ($M_w$ 5–6, focal depths 5–10 km) produced by non-exposed faults within the "competent group" above the Hormuz salt, which account for about half of the earthquakes; and (2) large-sized earthquakes ($M_w > 6$, focal depths >10 km) sourced from basement faults that can also rupture through the Hormuz salt and involve the cover. These events commonly occur associated with asymmetric SE-verging anticlines that show rare exposures of old formations and accommodate large vertical stratigraphic separations. Karasözen et al. (2019), using a multiple-earthquake relocation technique, analyzed the spatial distribution of seismicity across the Zagros Belt using ca. 2500 relocated earthquakes (location errors <5 km) spanning ca. 70 years of instrumental record (1951–2018), with calibrated focal depth data for ~1000 of them. Seismicity is constrained within a depth range of 4–25 km, with a peak in the depth distribution at 10–13 km, and earthquakes nucleated either in the basement or within the cover overlying the Hormuz salt. Fig. 2 shows the distribution of the relocated earthquakes of the catalog produced by Karasözen et al. (2019) in the Fars Arc. Here, instrumental seismicity shows a rather scattered distribution, mainly associated with the younger southern sector of the orogenic wedge, within a low-elevation belt (<1250 m a.s.l.) around 100–150 km wide N of the deformation front (Nissen et al., 2011; Karasözen et al., 2019). Almost all of the earthquakes in the central sector of the Fars Arc are related to reverse faults, whereas strike-slip focal mechanisms represent a significant proportion of the earthquakes in the western sector. Moreover, as shows the plot of calibrated focal depths, around half of the reverse and strike-slip earthquakes are nucleated within the "competent group" above the Hormuz salt.

The hillshade in Fig. 3 shows the tectonic and geomorphic setting of the Emad Deh rock avalanche, associated with the Gavbast anticlinal ridge and a buried diapir expressed as an inflated domal morphostructure superimposed on the anticline. The epicenters from the historical (1900–2005; Berberian, 2014) and instrumental (2006–2022; Iranian Seismological Center) catalogues indicate the high frequency of damaging earthquakes (Ms 5–6.2) in this area associated with the inferred Mountain Front Fault (Berberian, 1995). These include the 1880 $M_s$ 5.5 Jonah (or Jenah) and the 1956 $M_s$ 6.2 Gowdeh earthquakes, which caused >100 and 410 fatalities, respectively. Lohman and Simons (2005) and Barnhart et al. (2013), inverting InSAR-derived surface deformation data, ascribed the earthquakes of $M_w$ 5–5.8 located south of the Emad Deh rock avalanche, in the vicinity of the inferred Mountain Front Fault and Kemseshk diapir, to fault ruptures restricted to the supra-salt cover.

### 2.4. The tectonic landscape and drainage network development

The emergence of marine environments and the onset of the creation of topographic relief by differential vertical deformation related to folding constitutes a crucial landmark in the geomorphic evolution of each sector of the Simply Folded Belt. This is a diachronous process that advanced progressively towards the SW with the propagation of the deformation front and the incorporation of foreland sediments into the uplifting orogenic wedge. This major landscape change driven by tectonics is essentially recorded by the time-transgressive basal unconformity of the Bakhtyari Formation (Hessami et al., 2001; Mouthereau et al., 2007). These synorogenic alluvial deposits dominated by

conglomerates and commonly confined to synclinal depressions, provide evidence of a new landscape with significant topographic relief, comprising growing and laterally-propagating anticlinal ridges, and intervening synclinal depressions affected by relative subsidence. Within this morpho-tectonic setting governed by active detachment folding, the drainage network tends to be dominated by longitudinal streams confined along synclinal valleys. These strike drainages may either correspond to: (1) a newly formed river network developed on emerged land (Leturmy et al., 2010); or (2) to a pre-existing transverse drainage net, probably developed across an unconfined SW-sloping piedmont area (taper angle) that was deflected by the growing and laterally propagating anticlines (Mouthereau et al., 2007; Ramsey et al., 2008; Brettis et al., 2011). Water gaps and wind gaps carved across some anticlinal ridges are legacies of antecedent transverse drainages with sufficient downcutting capability to maintain their flow path, at least temporarily (Oberlander, 1985; Burberry et al., 2008, 2010; Collignon et al., 2016). As illustrates Fig. 2, the Fars Arc is essentially divided into three drainage basins dominated by longitudinal streams. The two largest ones are those of the Rud-e Shur and the Rud-e Mand that drain most of the eastern and western portions of the arc, respectively. A third catchment with smaller area occurs in the southernmost portion of the Fars Arc, drained by the Rud-e Mehran (Leturmy et al., 2010). Interestingly, the Gavbast Anticline lies at the junction of the divides of these major watersheds, suggesting that it corresponds to an important morpho-structure with prime importance in the configuration of the drainage.

## 3. Methodology

Geological-geomorphological maps of the Emad Deh rock avalanche and the associated portion of the Gavbast Anticline, including the Gavbast Dome, where produced following a phased approach. Initially, preliminary maps were drafted by the interpretation of: (1) stereoscopic greyscale aerial photographs from 1956 printed at an approximate scale of 1:40,000; (2) shaded relief models derived from TanDEM-X DEMs with a spatial resolution of 12 m; and (3) satellite images from GoogleEarth with spatial resolutions better than 5 m. In a subsequent stage, field surveys were conducted to refine the maps and collect data and samples. Field work was carried out with the aid of satellite images uploaded in a tablet with a GPS sensor. Morphometric parameters were extracted from the TanDEM-X DEMs. These DEMs, provided by the German Aerospace Center (DLR), are derived from bistatic X-Band interferometric SAR data acquired by the satellites TanDEM-X (TDX) and TerraSAR-X (TSX). Elevations are defined with respect to the reflective surface of X-Band interferometric SAR returns. This implies, together with the sparse vegetation of the study area (ca. 100–200 mm/yr average precipitation), that the used DEMs essentially represent Digital Surface Models. TanDEM-X DEMs use the WGS84 datum and have a nominal pixel spacing of 12 m, absolute vertical accuracies of $<$10 m (90 % confidence interval), a relative vertical accuracy of 2–4 cm (90 % confidence interval) (Wessel, 2016).

Two Optically Stimulated Luminescence (OSL) samples were collected from deformed alluvium underlying the rock avalanche deposits, driving opaque PVC tubes into sandy beds preventing exposure to light. Additionally, bulk sediment samples were obtained from around the sampling points for dose rate estimates. Ages were determined using the relation Age (ka) = equivalent dose (Gy)/dose rate (Gy/ka). Total dose rates were assessed: (1) measuring the activity concentrations of $^{238}$U, $^{232}$Th and $^{40}$K by high resolution gamma spectrometry (Radioisotopes Unit, University of Seville) and applying appropriate conversion factors (Guerin et al., 2011) (Table 1); (2) considering the water content of the samples on arrival at the laboratory plus a 5 % error, to account for radiation attenuation and variability; and (3) calculating the contribution of cosmic radiation as a function of latitude, altitude, burial depth, and average overburden density, based on data from Prescott and Hutton (1994). Final dose rate values were calculated using DRAC calculator (Durcan et al., 2015) (Table 1). Equivalent dose values were derived from optically stimulated luminescence (OSL) measurements on quartz grains of sizes 150–250 μm extracted from each sample. A total of 24–48 multi-grain aliquots of each sample were measured using a SAR blue OSL protocol (University of Cologne, Germany). Dose distribution showed over-dispersion values of 17 % for sample ED-U and 30 % for sample ED-M (see graphs with dose distributions in Supplementary Material). Outliers within the dose population have been identified as those values outside 1.5 times the Inter Quartile Range and have been excluded from the burial dose estimation. The Central Age Model (CAM, Galbraith et al., 1999) on the reduced dose population has been applied to estimate the burial dose. The ages are expressed as kiloyears before 2019 (Table 1).

## 4. The growth of the Gavbast anticline and dome

The Emad Deh rock avalanche was initiated as a planar rockslide on the northern limb of the Gavbast Anticline, and at the NW edge of the Gavbast Dome related to a buried salt stock (Figs. 3, 4). The Gavbast Anticline is located in the southern-central sector of the Fars Arc, north of the Mountain Front Fault inferred by Berberian (1995), and relatively close to the Deformation Front of the mountain belt (Fig. 2). Here, the folds have a dominant WNW-ESE trend and are pierced by numerous salt diapirs. Most of the diapirs have emerged at the surface producing salt extrusions, while others are expressed as structural domes superimposed on anticlines above buried salt stocks (Jahani et al., 2007, 2009). The WNW-ESE oriented Gavbast Anticline has a relatively complex geometry (Fig. 3). East of the Gavbast Dome it displays a sinuous axial trace, probably related to deflections during fold propagation towards the weak zones associated with two salt diapirs; Gavbast and the salt extrusion that pierces the eastern pericline (Callot et al., 2007; Jahani et al., 2009). At Gavbast Dome, the anticline has experienced significant vertical and lateral inflation related to the rise of the buried salt stock, as revealed by variations in the strike and dip of the strata, the widening of the fold, and the upward bulging of the anticline crest (Fig. 4). The strata and the slopes, especially on the northern limb, have been oversteepened and their cartographic trace displays outward deflections away from the fold axis. Differential uplift of the overburden by salt rise has resulted in the development of an ellipsoidal morpho-structural dome around 22 km in axial length, which forms the highest mountain in the region (Kuh-e Gavbast; 2165 m a.s.l.). The topographic surface of the dome largely coincides with the top of the limestones of the Khami Group (Lower Cretaceous), strongly indurated by a hardground, and the top of the carbonate rocks of the Bangestan Group (Fig. 4). These

**Table 1**
Radionuclide activity concentration measured by high resolution gamma spectrometry. Sample depth and assigned water content for total dose rate calculation are indicated. A ± 5 % water content has been added to account for variability over the burial time. Total dose rates, estimated burial doses and derived ages.

| Sample | Lab code Cologne/ Sevilla | Depth (m) | Moisture (%) | $^{40}$K (Bq/kg) | $^{232}$Th (Bq/kg) | $^{238}$U (Bq/kg) | Dose rate (Gy/ka) | Burial dose (Gy) | Age (ka before 2019) |
|---|---|---|---|---|---|---|---|---|---|
| ED-M | C-L4985 4175 | 1.1 | 13 | 228 ± 23 | 10 ± 1 | 32 ± 2 | 1.53 ± 0.08 | 11.3 ± 0.6 | 7.4 ± 0.5 |
| ED-U | C-L4986 4176 | 0.4 | 13 | 139 ± 7 | 7 ± 2 | 40 ± 2 | 1.42 ± 0.06 | 7.7 ± 0.4 | 5.4 ± 0.3 |

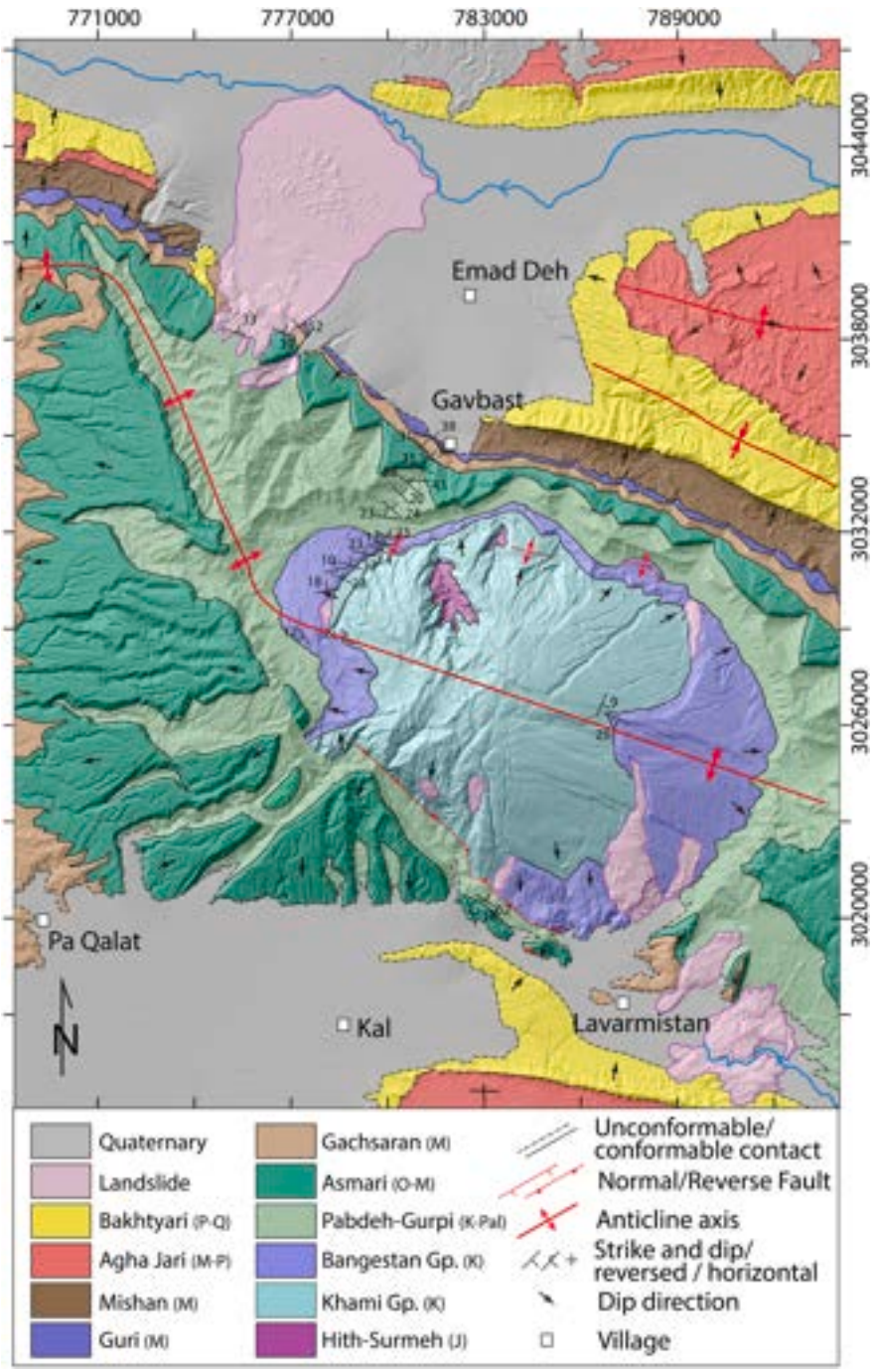


**Fig. 4.** Geological map showing the position of the Emad Deh rock avalanche on the NE limb of the Gavbast Anticline and at around the NW edge of the Gavbast Dome, related to a buried stock of Hormuz salt. The map also shows other landslides associated with the Gavbast Dome, including a large rockslide-avalanche developed on Pabdeh marls and limestones that blocked a drainage E of Lavarmistan village.

are bulged stratigraphic surfaces exhumed after the removal of a thick succession (Pabdeh-Gurpi, Asmari, Fars Group). Moreover, Gavbast Dome includes the oldest formations exposed in this sector of the Fars Arc, with the base of the outcropping stratigraphic succession starting with the Hith and Surmeh formations (Perry et al., 1965). The dome is affected by fresh-looking normal faults with dominant fold-parallel and fold-normal trends attributable to radial extension related to active uplift and arching (Jackson and Hudec, 2017). The elevation difference of the top of the Khami Group in the dome and along the fold axis, reconstructed from a longitudinal cross section, indicates a vertical uplift related to diapiric rise of around 1100 m. Jahani et al. (2007, 2009), based on cartographic data, a seismic line acquired across the Gavbast Dome and field observations, interpret that the Gavbast Anticline is a salt-cored detachment fold involving a supra-salt cover around 11 km thick. These authors also indicate that the buried salt stock is currently experiencing rejuvenation by tectonic shortening.

West of the dome, the Gavbast Anticline splits into two narrow anticlines and a broad intervening syncline (Fig. 3). The W plunging pericline of the syncline associated with the western edge of Gavbast Dome is expressed as a broad planar dip slope. The northern anticline displays two sections with NW-SE and *E*-W trends separated by a sharp inflection. The rock failure that led to the Emad Deh rock avalanche occurred on the NE limb of the NW-SE oriented portion of this northern anticline associated with the Gavbast Dome (Fig. 4). Here, the structural

dome has a vague edge, which could be located at or next to the Emad Deh rock failure. The southern anticline, designated as Varavi, extends along 130 km to the east and displays an asymmetric geometry with a steeper southern limb (Burberry et al., 2008, 2010) (Fig. 2).

The area displays an overall concordant topography, comprising anticlinal ridges separated by synclinal depressions (Figs. 2, 3). The depressions are characterized by coalescing gravelly alluvial fans on both margins and longitudinal drainages that may display relatively wide floodplains and salt flats. The Quaternary alluvial-fluvial deposits are mainly underlain by sediments of the Fars Group and the Bakhtyari Formation, including units with contrasting rheology. Geological mapping carried out in the area and the examination of shaded relief models revealed that the alluvial fan surfaces are offset at numerous sites by strike-parallel flexural-slip faults, expressed as upslope-facing scarps (see location in Fig. 3). These fresh-looking surface ruptures related to bedding-parallel faults in the bedrock that offset the unconformable Quaternary cover provide clear evidence of active folding (Rockwell 1988; Walker et al., 2005; Walker et al., 2015; Gutiérrez et al., 2014; McCalpin et al., 2020), involving relief rejuvenation in the anticline ridges and the steepening of the strata and the slopes.

The local relief between the anticlinal ridges and the intervening synclinal depressions depends on: (1) differential vertical displacement related to folding, and locally diapiric rise; (2) aggradation, or rarely fluvial incision in the synclinal depressions; and (3) erosion along the crest of the ridges. The erosional unroofing of the anticlinal ridges can proceed at high rates on soft sediments of the Fars Group (Agha Jari, Mishan, Gachsaran formations), until it reaches the resistant Asmari Limestone, which often forms the carapace of the paradigmatic whaleback anticlines of the Zagros (Fig. 3). The elevation difference between the anticlinal ridges and the synclinal valleys provide a minimum measure of the differential vertical displacement related to folding. The onset of this morphogenetic folding process can be roughly situated in each sector of the Simply Folded Belt at the base of the Bakhtyari Formation. Mouthereau et al. (2007), based on the magnetostratigraphic age of the base of the Bakhtyari Formation in the frontal sector of the Simply Folded Belt (Lurestan Arc; Homke et al., 2004), suggest that folds in the southern sector of the Fars Arc became emergent at ca. 3–2 Ma. The elevation difference between the crest of the Gavbast Anticline on both sides of the Gavbast Dome (ca. 1800 m a.s.l.) and the floor of the northern (630 m a.s.l.) and southern valleys (370 m a.s.l.) are 1170 m and 1430 m, respectively. These values indicate minimum differential vertical displacement rates related to tectonic folding of 0.4–0.7 mm/yr, assuming that the topographic growth of the folds started at ca. 3–2 Ma. Similar values of 0.3–0.6 mm/yr were estimated by Mouthereau et al. (2007) in folds of the central-western sector of the Fars Arc. The actual rates can be significantly higher considering that both erosion and aggradation may have reduced substantially the total vertical displacement. As indicated above, the Gavbast Dome shows a local structural relief related to salt rise of approximately 1100 m. Hence, the minimum vertical displacement related to both folding and diapiric rise at the crest of the dome with respect to the northern and southern valley reach values of 2270 and 2530 m, respectively. These figures yield minimum uplift rates related to both folding and diapiric rise of 0.8–1.3 mm/yr (at the dome crest), assuming that the deformation started at ca. 3–2 Ma.

The Gavbast Anticline displays three features suggesting that it may be underlain by a N-dipping reverse basement fault (Fig. 3): (1) In contrast with the dominant symmetric geometry of the anticlines in the Fars Arc (Jahani et al., 2009), Gavbast Anticline is a markedly asymmetric fold with a steeper southern limb. This asymmetry is clearly displayed in the fold section east of the Gavbast Dome and in the two narrow anticlines that splay west of the dome. (2) The two adjacent synclinal depressions show a significant down-to-the-south topographic drop of around 300 m, indicating differential vertical displacement on both sides of the anticline. (3) As explained above, the Gavbast Anticline controls the position of the main watershed divides in the Fars Arc, suggesting particularly high uplift rates ascribable to both supra-salt detachment folding and dip slip displacement on a blind basement reverse fault.

## 5. The rock avalanche and the associated landslides

### 5.1. The source of the landslides

The source of the Emad Deh rock avalanche and the subsequent landslides (L2-L5) nested between the lateral levees of the former, is located on a dip slope at the NE limb of the northern anticline that splays from Gavbast Anticline (Figs. 4, 6). This section of the fold is situated at the vaguely-defined NW edge of the Gavbast Dome. Here, the resistant Asmari Limestone has been eroded from the crest of the breached anticlinal ridge, and a deeply entrenched longitudinal valley (*combe*) has been excavated along the axis of the fold into the soft marl-dominated Pabdeh and Gurpi formations. This implies that the bedding planes of the slid strata daylight at the back antidip slope (Fig. 5). The formations affected by the multiple slope failures have a 35–40 NE dip and include from base to top the following conformable units (Figs. 5, 7A, D): (1) upper ca. 60 m of the Pabdeh Formation, consisting of light grey marls with intercalations of limestone beds, significantly more frequent towards the top; (2) the mechanically resistant and massive brown to reddish brown Asmari Limestone, with a total thickness of approximately 180 m; (3) gypsum with marls, claystones and limestone intercalations of the Gachasaran Formation, around 250 m thick; and (4) cream-colored fossiliferous limestones 80 m thick of the Guri Member of the Mishan Formation. West of the rock avalanche, a patch of Bakhtyari conglomerates unconformably overlie rocks of the Asmari, Gachsaran and Guri formations. The geological map shows that the Emad Deh rock avalanche was sourced from a dip slope on Asmari Limestone, plus small ridges (hogbacks) in the lower part of the mountain front formed by the Gachsaran Formation and the Guri Member (Fig. 5). In this sector of the anticline, the top of the resistant Guri limestone controls a linear mountain-piedmont junction related to differential erosion of the soft Mishan and Agha Jari formations, which are concealed by Quaternary deposits. The NE limb of the anticline is deeply dissected by transverse drainages that have created large intervening flatirons of Asmari Limestone. The steep drainages feed coalescing alluvial fans in the piedmont of different generations, expressed as higher entrenched surfaces (east of the avalanche) and lower active surfaces (west of the avalanche). The alluvial fans grade distally into the floodplain of the longitudinal stream that flows along the synclinal depression.

The slope that sourced the landslides had a local relief of 850 m and an overall slope of 21°, measured from the crest of the ridge at the margins of the scar to the foot of the range front (Fig. 6). The scar generated by the Emad Deh rock avalanche and the subsequent slope failures has penetrated up to a laterally continuous limestone bed of the Paddeh Formation, situated around 60 m below its top contact with the Asmari Formation (Figs. 5, 7A, B). The exposed sliding surface is designated by the local people with the Farsi word “chaksafid”, meaning white wall. This extremely planar basal failure plane is largely covered by recent colluvial debris, but it can be observed where the slope deposits have been eroded (Fig. 7A, B). In the recently exhumed portions it displays well-defined dip-parallel grooves and striations, which may correspond to slickensides related to both, friction created by a sliding mass, and flexural folding. In the sectors where the plane has been exposed over longer time, the slickensides have been largely obliterated by solution features, including irregular etching, pitting and solution runnels (De Waele and Gutiérrez, 2002) (Fig. 7B). The lower part of the sliding surface is buried by landslides L3 and L5 (Fig. 5). The boundaries of the scar are defined by the crest of the dip slope (hogback) and nearly vertical lateral scarps up to 160 m high perpendicular to the strike of the bedding, most probably controlled by deep-penetrating transverse joints that can be recognized in adjacent areas (Fig. 7A, D). The lateral edges of the scar in the lower part of the slope corresponds to a flatiron of Asmari Limestone on the SE, and outcrops of Gachasaran Formation on the NW

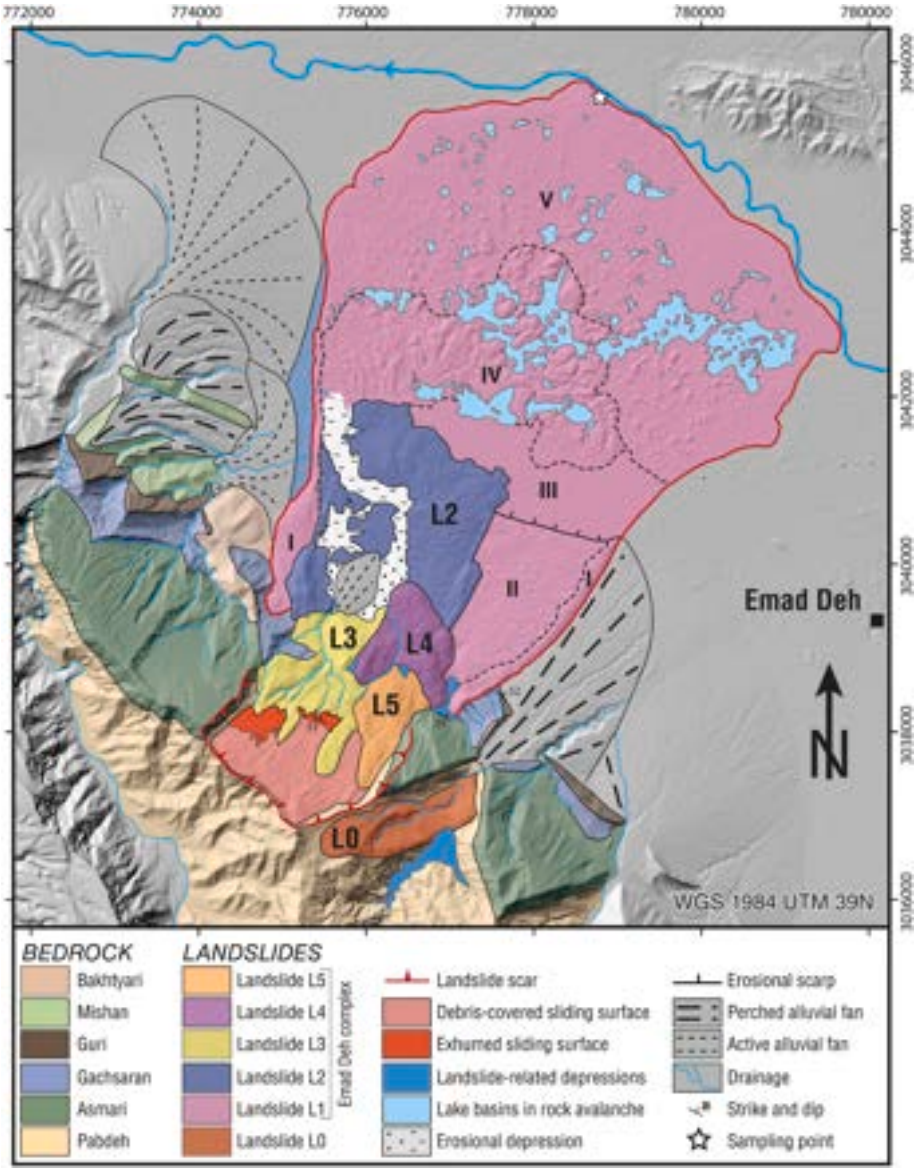


**Fig. 5.** Geological-geomorphological map of the Emad Deh rock avalanche (L1) and subsequent landslides (L2-L5) nested between the lateral levees of the former. The deposits of the Emad Deh rock avalanche are divided into five domains with different morphological features that reflect the variability of the behavior of the flow that travelled over sloping coalescing alluvial fans and flat, soft, water-saturated floodplain deposits.

**Fig. 6.** Frontal panoramic view of the Emad Deh rock avalanche and its geomorphic context. Arrows indicate the lateral edges of the scar. Note conical hills (hummocks) accumulated in the distal sector on floodplain deposits, where the avalanche experienced significant radial spreading.

(Fig. 5). It displays a downslope widening trapezoidal geometry in plan, with a variable width of 1690 to 2100 m. The scar has a horizontal length of 1880 m in the slope direction, measured from the crest to the mountain-piedmont junction, and planimetric area of 3.7 $km^2$.

The approximate aggregate volume of rock mass evacuated from the scar by the multiple landslides (L1-L5) has been roughly estimated at 420 $Mm^3$ multiplying the average width of the scar (1950 m) by the average lateral area of the detached rock slab. The latter value has been computed from the mean of the areas of the two flanks of the scar, assuming that the basal failure has a constant dip of 35° up to its

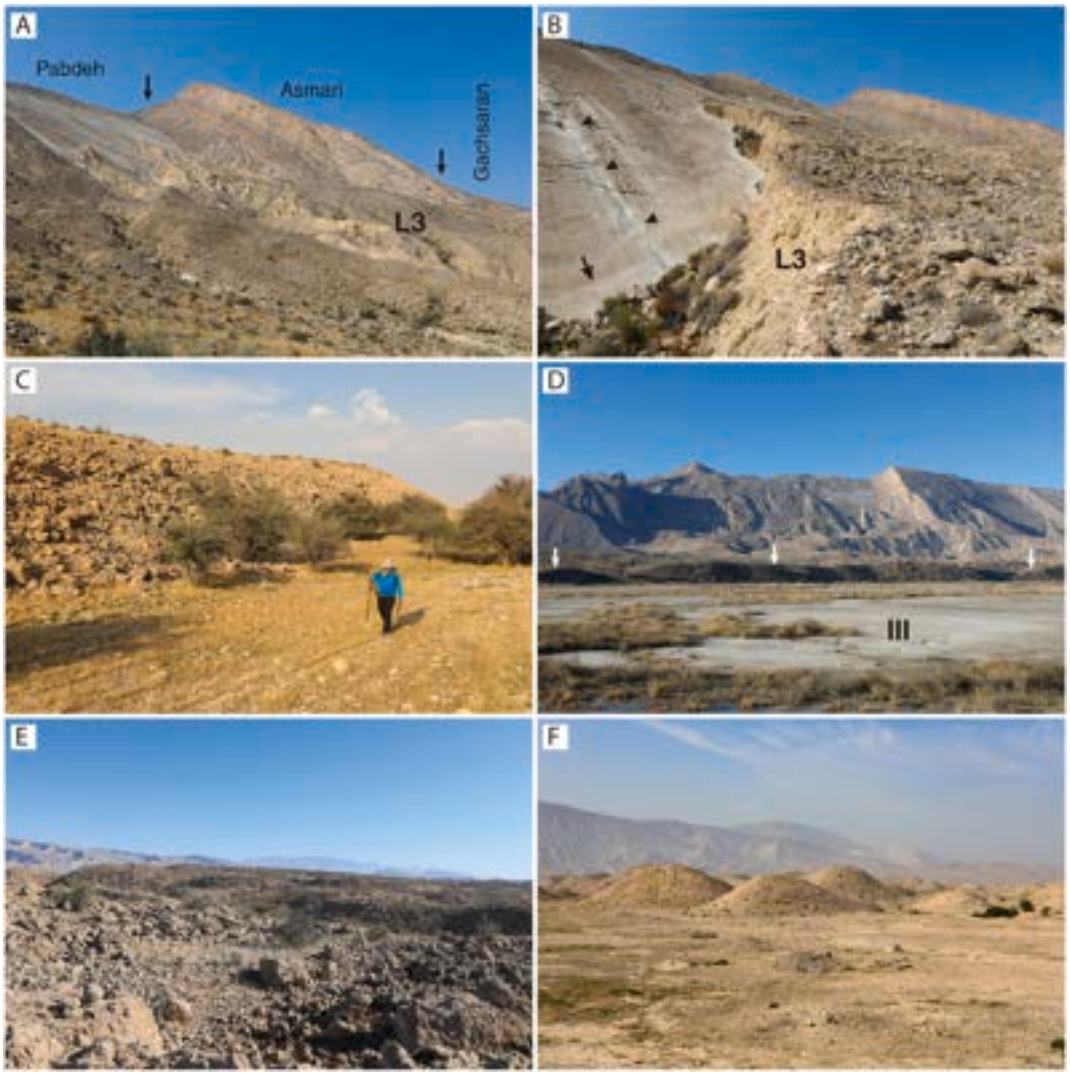


**Fig. 7.** Images of the Emad Deh rock avalanche. A: View of the scar created by the Emad Deh rock avalanche and the subsequent slope failures, affecting Pabdeh (marls with limestone intercalations), Asmari (resistant limestone), and Gachsaran (gypsum) formations. The exposed failure surface corresponds to the top of a limestone bed in the upper part of the Pabdeh Formation. B: Close-up view of the exhumed basal sliding surface showing dip-slip striations (arrow) and solution features such as irregular etching and solution runnels (arrow heads). Upper edge of landslide L3 on the right. C: Outer free-standing side of the right lateral levee of the Emad Deh rock avalanche with its surface studded by large boulders. D: View of the scar, the downslope scarped edge of the proximal rock avalanche deposit (labelled as II in Fig. 5, white arrows) and the depression with fine-grained post-avalanche deposits in the foreground (labelled as III in Fig. 5). E: Domain dominated by polygonal hills (labelled as IV in Fig. 5) showing a flat top sloping towards the source and a carapace of large boulders. F: Conical hills in the distal domain of the rock avalanche deposit (labelled as V in Fig. 5).

emergence at the mountain-piedmont junction. The main uncertainty associated with this calculation is related to the implicit assumption whereby the slope used to have an essentially non-dissected, laterally continuous geometry. The measured values for the lateral areas indicate that the total rock volume evacuated for the scar had an average bedding-normal thickness of 90–95 m.

### 5.2. The rock avalanche deposit

The Emad Deh rock avalanche deposit was accumulated in the piedmont on coalescing alluvial fans and the floodplain (Fig. 5). It displays a 7750 m long lobate form in plan, covering 31.62 km$^2$. The avalanche deposit deflected to the north the west-flowing longitudinal stream that drains the valley, but did not reach the opposite margin (i.e., no frontal confinement). The rock avalanche has a maximal height drop (H) of 914 m and a runout (L) of 9280 m. These parameters are given by the vertical and planimetric distances between the crown of the head-scar and the distal edge of the deposit, respectively, yielding a H/L mobility index of 0.09 and a travel angle of 5.6°. These figures indicate that the Emad Deh rock avalanche experienced an extraordinarily high mobility, compared with the values computed for a large number of rock avalanches worldwide (e.g., Aaron and McDougall, 2019; Strom et al., 2019).

The avalanche deposit in its proximal sector was accumulated between two alluvial fans with convex cross profiles, filling the trough in the interfan area. The alluvial fan on the east corresponds to an older and higher surface, imposing a stronger lateral confinement to the flow of fragmented rock (Fig. 5). The medial axis of the lobe-shaped avalanche deposit displays a westward deflection of 15° with respect to the expected travel direction given by the orientation of the scar and the dip of the bedding-controlled sliding surface. It seems that higher interference with the more prominent fan deposits on the east side induced a westward cross-tilt in the debris stream and its deflection. A similar situation was described by Blair (1999) in the North Long John rock avalanche of the Inyo Mountain piedmont in Owens Valley, California. The width of the avalanche deposit expands from 2695 m at the

proximal tip of its lateral levees, to 6150 m across its widest sector (expansion factor of 2.3) (Fig. 5). The most significant expansion occurred downslope of the coalescing alluvial fans that partially confined the flow along the interfan trough. Downslope, the avalanche spread over a flat floodplain surface underlain soft deposits with a shallow water table.

A minimum volume of 224 $Mm^3$ has been estimated for the rock avalanche deposit multiplying the area of the deposit (31.62 $km^2$) by a minimum average thickness (7.1 m). The latter value has been calculated: (1) computing the average thickness of the deposit in six cross sections assuming a planar base; and (2) calculating the average thickness from the values of each section weighted for the length of the section. This minimum value is much lower than that expected from the volume of the scar, indicating that a substantial part of the rock avalanche deposit fills the buried interfan trough. More reliable volume estimates of 350 $Mm^3$ (rock mass at the source) and 420 $Mm^3$ (avalanche deposit, 20 % bulking factor) have been obtained considering the volume of the scar (420 $Mm^3$) generated by the multiple failures and the aggregate volume of landslides L2 to L5 (84 $Mm^3$ the deposits, and 70 $Mm^3$ the rock mass at the source). The volume of the Emad Deh rock mass at the source (350 $Mm^3$) is given by the volume of the scar (420 $Mm^3$) minus the aggregate volume of landslides L2 to L5 at the source (70 $Mm^3$).

Restricted exposures of the avalanche deposit were examined in some artificial excavations and steep erosional slopes located in the lateral levees and the hummocks of the distal sector, unfortunately none of them reaching the base (Fig. 8A, B). In both contexts the deposits consist of a strongly comminuted, angular, unsorted and chaotic cobbly pebble gravel with scattered boulders and variable amounts of muddy matrix (mostly packbreccia and locally floatbreccia). This main body is capped by a matrix-free carapace of large blocks up to several meters long. The breccia underlying the carapace includes limestone clasts of Pabdeh and Asmari limestone, indicating that the basal sliding surface of the collapsed slab the led to the Emad Deh rock avalanche was situated within the Pabdeh Formation. The "survivor" limestone boulders embedded in the main breccia can be extensively fractured (jigsaw crackle breccia). The matrix is dominated by a light grey pulverized muddy material largely derived from the marly Pabdeh and the gypsiferous Gachsaran formations. Interestingly, this matrix-bearing breccia locally displays some pseudo-bedding with undulating geometries expressed by net vertical changes in colour, grain size and matrix content (Fig. 8A, B). The carapace is dominated by blocks of Asmari Limestone, which surface displays a reddish brown varnish and extensive post-depositional solutional etching and pitting. The predominance of Asmari Limestone blocks at the surface suggests that the stratigraphic sequence in the source slope was retained in the rock avalanche until its deposition, as it has been observed in a number of case studies (e.g., Hewitt et al., 2008; Dufresne et al., 2016). Moreover, the overall reverse grading supports the concept whereby dispersive pressure related to particle-particle interaction and fragmentation tends to lift and maintain the coarsest clasts at the top of the granular flow (kinetic sieving; e.g., Bagnold, 1954; Blair, 1999).

The accumulation area of the avalanche displays three sectors with distinctive morphological features attributable to different flow-depositional behavior (Fig. 5): (A) proximal area with paired lateral levees (I) and an inner sheet-like deposit (II); (B) intermediate depression (III); (3) polygonal hills (IV); and (4) conical hills (V).

In the proximal area, the avalanche deposit displays well-defined lateral levees studded by large boulders of Asmari Limestone on the surface (labelled as I in Fig. 5, Fig. 7C). These deposits were sheared off from the descending rock avalanche in response to lateral friction with the adjoining alluvial fans. The levees show a considerable outward offset with respect to the lateral edges of the scar at the foot of the mountain front, indicating rapid disintegration and expansion of the collapsed slab in the initial section of its travel path. The 3.9 km long left levee has an overall slope of 1.3° and reaches a height of 31 m above the adjoining alluvial fan. It shows a wider proximal section (up to 450 m wide) associated with steeper ground on bedrock associated with the range front, which imposed a greater restraining effect on the flow, and a narrow medial-distal section. In the medial sector, the inner side is cut by a sharp erosional scarp indicating that the nested landslide L2 was confined by the levee and bulldozed some of its deposits. The avalanche deposit created a linear depression between the western alluvial fans and the left levee, which is partially filled by fine-grained deposits. Probably, this was initially an internally drained trough that was open by overfilling and/or erosion. The right levee is 3.2 km long, has a

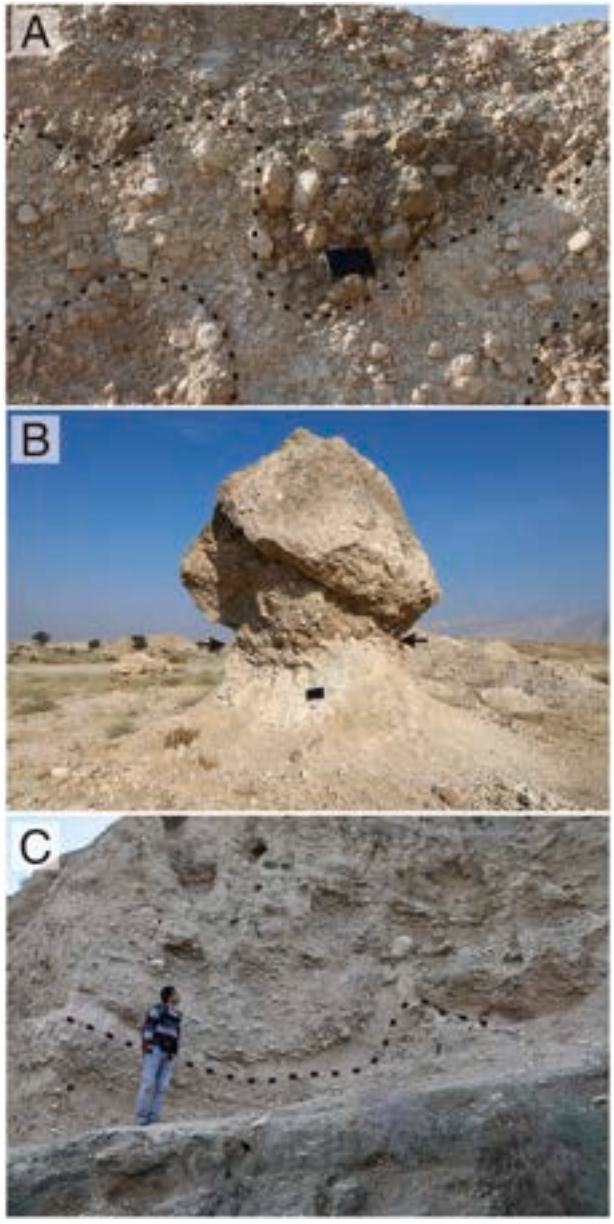


**Fig. 8.** Images of rock avalanche deposits and the alluvium on which the avalanche was deposited at its distal sector. A: Exposure at the distal edge of the right lateral levee, showing angular, unsorted crushed cobbly pebble gravel with pulverized muddy matrix. Dashed lines indicate undulated pseudo-bedding. Notebook 21 cm long. B: Pedestal formed by differential erosion of avalanche deposits, consisting of an upper carapace of large blocks and a main body of gravel breccia with muddy matrix. The capping block is derived from Asmari Limestone. Arrows point to a net discontinuity that separates units with different colour and texture. Notebook 21 cm long. C: Exposure at the distal edge of the rock avalanche showing alluvium folded by the sudden load exerted by the rock avalanche on soft substratum.

significantly higher overall longitudinal gradient of 2.8°, and reaches a local relief of 28 m above the external ground (Fig. 7C). In the proximal sector, this levee defeated several NW-directed drainages, creating small closed depressions with a fill of fine-grained deposits (Fig. 5).

In the proximal sector, between the lateral levees, the avalanche deposit displays a sloping surface 2.3 km long with a general slope of 3.1° and a carapace of meter-sized boulders (labelled as II in Fig. 5). This portion of the avalanche deposit has been buried by landslide L2 on its central and western sector, and terminates abruptly at its downslope edge by a puzzling rectilinear downslope-facing scarp 20–25 m high (Fig. 7D). This depositional surface shows a crenulated geometry with transverse, discontinuous troughs and ridges of meter-sized relief and convex-up arcuate traces. The position of the distal edge coincides with the boundary between the steep western alluvial fan and the floodplain, and hence with a slope break and a change in the nature of the substrate.

In the intermediate sector, beyond the continuous proximal avalanche deposit, there is a transverse depression 1.3 km wide (labelled as III in Fig. 5) underlain by post-avalanche fine-grained sediments (lacustrine, sheet wash, aeolian) (Fig. 7D). The depression has a very linear southern edge buried on its western sector by landslide L2 and a sinuous northern margin. The flat floor is locally interrupted by scattered hillocks of rock avalanche breccia. The depression, together with the sharp distal termination of the avalanche deposits situated upslope (domain II), record a section in the flow path in which the avalanche did not produce any significant accumulation, and probably caused some erosion in the soft floodplain deposits. This sharp change in the morpho-sedimentary style was probably related to the associated variation in substrate and gradient; from a sloping fan underlain by indurated gravels to flat floodplain with soft and water-saturated deposits.

Two different geomorphic styles have been differentiated in the hilly distal sector of the rock avalanche, where the flow experienced its greatest lateral radial expansion (Fig. 5). In the sector situated beyond the depression, the rock avalanche deposit is dominated by flat-topped polygonal hills with an overall uphill-facing slope of 2.3° (labelled as IV in Fig. 5; Figs. 7E, 9A). The top of these hills displays a carapace of matrix-free boulders, and is designated by the local people as “kerah”, meaning area with large blocks. This domain is 4.2 km wide and reaches a maximal length of 2.4 km in the medial zone of the lobe. The hills are separated by narrow longitudinal and transverse troughs (Fig. 9A). The flow-parallel, often radially oriented troughs are mostly rectilinear, while the flow-transverse troughs have a dominant arcuate geometry with the concavity facing downflow. This pattern seems to reflect the breakup of a continuous debris stream into portions along discrete longitudinal and transverse zones in response to extensional flow and radial spreading (Dufresne and Davies, 2009). The irregularly-edged low-lying areas intervening the flat-topped hills are underlain by fine-grained secondary deposits mostly derived from the selective erosion (winnowing) of the matrix of the rock avalanche deposit.

The most distal sector of the rock avalanche lobe is characterized by a hummocky topography consisting of conical hills with rounded tops (labelled as V in Fig. 5). This sector is known as “tolestan” by the local people, meaning hilly area (Figs. 6, 7F, 9B). These hills display a broad range of morphologies, ranging from isolated conical hums to more complex hills with linear to irregular shape in plan, and multiple conical culminations and intervening saddles (Fig. 9B). For the sake of simplicity they can be described as single and compound conical hills. The hills in this domain show the following general features (Figs. 9B, 10A): (1) the linear compound hills and the aligned hills tend to show a radial-longitudinal orientation; (2) the relative frequency of the single hills increases in the distal direction, indicative of a greater breakup of the debris stream related to radial spreading; (3) the size of the hills show a progressive decrease towards the distal edge of the deposit. A total of 550 hummocks have been mapped with high resolution satellite images and a hillshade (Fig. 10A). Table 2 presents the main morphometric data of the mapped hummocks. The median values for the area, length and width are 3232 $m^2$, 78 m and 55 m, respectively. The

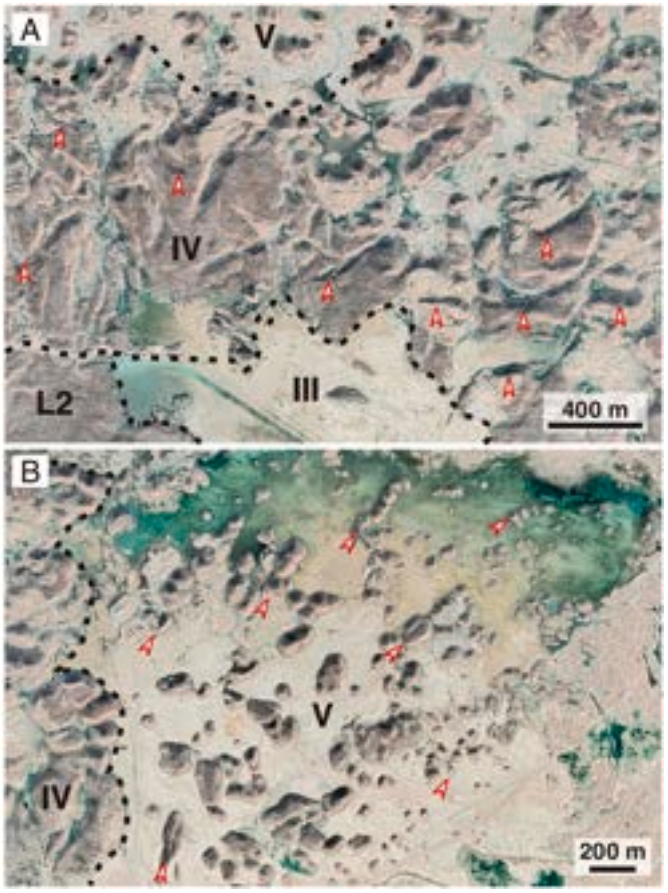


**Fig. 9.** Satellite images captured from Google Earth of the distal sector of the avalanche deposit, characterized by flat-topped polygonal hills (domain IV), conical hills (domain V), and intervening low-lying areas with ephemeral lakes and underlain by post-avalanche fine-grained deposits. A: Domain of polygonal hills (IV) situated between landslide L2 and the intermediate depression (III) to the south, and the conical hills (V) to the north. The polygonal hills are predominantly separated by troughs with longitudinal and transverse orientations (red arrowheads). The latter typically show an arcuate trace with the concavity facing downflow. B: Single and compound conical hills (V) east of the polygonal hills domain (IV) featuring radially aligned orientations and alignments, and a general decrease in size towards the distal edge of the deposit. (For interpretation of the references to colour in this figure legend, the reader is referred to the web version of this article.)

maximum and median heights of 33 and 5.9 m should be considered as minimum values, considering the degradation experienced by the hills, the aggradation occurred in the surrounding areas, and the resolution of the DEM (12 m). McColl and Davies (2011) measured heights of up to 15 m in the Hillocks rock avalanche at Otago, New Zealand. The average elongation ratio of around 1.4, plus the sinuosity index (i.e., ratio between the hill perimeter and the perimeter of a circle with the same perimeter) close to 1 indicates that a significant proportion of the hummocks are compound hills, but they have a dominant subcircular to ellipsoidal geometry in plan. The median of the aspect ratio (height to length ratio) of 0.07, which should be considered as a minimum estimate, is in agreement with the common aspect ratios of <0.1 indicated by Dufresne and Davies (2009). The rose diagram inset in Fig. 10A depicts the frequency of the orientation of the major axes of the 201 hills with elongation ratios higher than 1.5. The distribution of the azimuths show a wide dispersion compared with the arc defined by the direction of the lateral edges of the rock avalanche deposit (arrows), suggesting a significant transverse component in the radial spreading process (Dufresne and Davies, 2009).

The conical hills in domain V have an overall density of 30.1 hills/

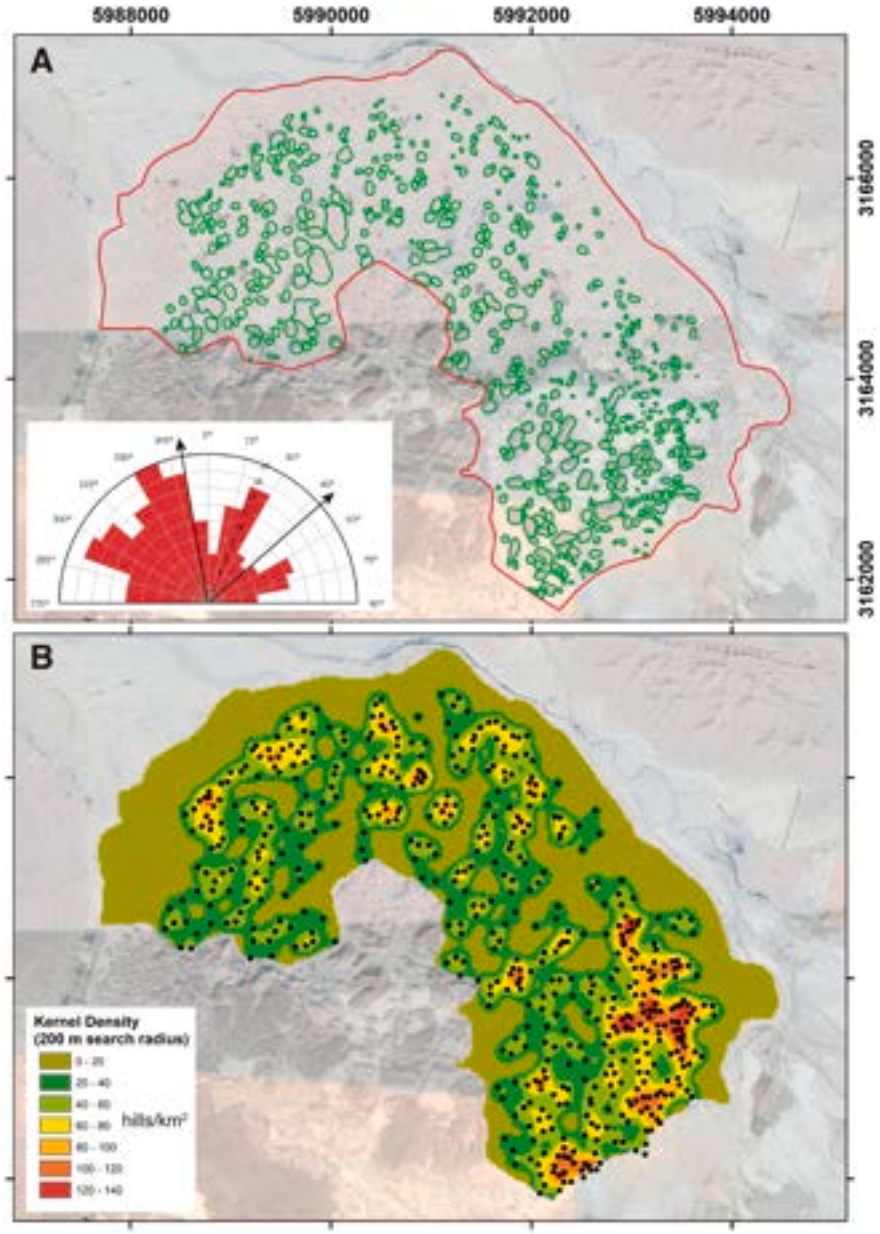


**Fig. 10.** Map and density model of the single and compound conical hills mapped in the distal domain (labelled as V in Fig. 5). A: Polygons representing the outline of the 550 mapped conical hills showing a progressive decrease in size towards the distal edge of the avalanche deposit. Inset rose diagram depicts the frequency of the orientation of the major axes of the 201 hills with elongation ratios higher than 1.5. Note the wide dispersion of the azimuths compared with the arc defined by the direction of the lateral edges of the rock avalanche deposit (arrows). B: Kernel density model generated with the centroid of the 550 hills, a search radius of 200 m and the minimum bounding area that encloses them. Note higher density in the flanks, and an overall random distribution with local clusters of radially aligned hummocks. (For interpretation of the references to colour in this figure legend, the reader is referred to the web version of this article.)

**Table 2**
Main morphometric parameters of the 550 single and compound conical hills.

| | Maximum | Minimum | Average | Standard deviation | Median |
|---|---|---|---|---|---|
| Area ($m^2$) | 74,302 | 91 | 5105 | 6773 | 3232 |
| Perimeter (m) | 1155 | 36 | 245 | 146 | 215 |
| Length (m) | 479 | 13 | 90 | 55 | 78 |
| Width (m) | 253 | 9 | 60 | 32 | 55 |
| Height (m) | 33 | | 6.9 | 5.5 | 5.9 |
| Elongation ratio | 3.2 | 1 | 1.47 | 0.33 | 1.38 |
| Aspect ratio | 0.2 | | 0.07 | 0.04 | 0.07 |
| Sinuosity | 1.6 | 1 | 1.08 | 0.08 | 1.05 |

$km^2$ (18.26 $km^2$ total area). A Kernel density model has been produced with the centroids of the hills and with a search radius of 200 m (Fig. 10B). This model illustrates that the hills reach higher densities in the central-distal sector of the domain, and especially at their flanks. It also shows that they have an overall random distribution with local clusters showing a rough radially aligned pattern. A nearest neighbor index (NNI) of 0.94 (z-score − 2.43; p-value 0.015) has been calculated for the centroids in the minimum bounding area that encloses them. This index allows the quantification of the degree of clustering versus dispersion of features distributed within a certain area, and varies from 0 to 2.1. A NNI equal to 2.15 indicates maximum dispersion with uniform hexagonal pattern, 1 perfect random distribution, and 0 maximum clustering (attached centroids) (Clark and Evans, 1954; De Waele and Gutiérrez, 2002). The obtained NNI confirms the overall random distribution. The flat areas intervening the hills are underlain by light-colored fine-grained deposits derived from the erosion of the hummocks. They include relatively large ephemeral lakes with highly sinuous outlines interrupted by protruding hummocks. The distal fringe of the avalanche deposit lacks hummocks and shows a low-relief corrugated topography with vague transverse ridges and troughs. The distal edge is slightly sinuous, with some frontal lobes, and is locally dissected by dense networks of gullies.

### 5.3. The chronology of the rock avalanche

At the distal edge of the rock avalanche deposit, the river has trimmed a steep scarp that exposes rounded, well-sorted and stratified fluvial deposits, overlain by angular, unsorted and massive avalanche breccia. The fluvial deposits consist of gravels with interbedded silt beds and are affected by N-verging folds with trends perpendicular to the avalanche flow direction (Fig. 8C). These soft-sediment deformations indicate that the avalanche was emplaced on mechanically weak water-saturated deposits in a floodplain environment, and that they were affected by folding soon after their deposition in response to the sudden N-directed loading induced by the avalanche. Dufresne et al. (2016) provides a compilation of case studies showing unconsolidated substrate affected by soft-sediment deformation, liquefaction, upward intrusions, or even its squeezing out and ejection (von Poschinger and Kippel, 2009).

Two samples were collected for OSL dating at point 39R 778819E 3,045,579 (labelled with an asterisk in Fig. 5) from two silt beds in the upper part of the fluvial package, capped by a rock avalanche deposit 1.5 m thick at this site. The upper sample ED-U was collected from a silt bed situated 1.1 m below the top of the fluvial succession, at 20.7 m above the foot of the scarp. The lower sample ED-M was obtained from a sandy silt bed 1.8 m below the alluvium-avalanche contact. The two sampled silt beds are separated by a well exposed folded bed of rounded pebble gravel. The samples have yielded OSL ages of 5.4 ± 0.3 ka (ED-U) and 7.4 ± 0.5 ka (ED-M) in correct stratigraphic order (Table 1). The age of the upper sample, which dose distribution showed a significantly lower over-dispersion (17 % versus 30 %), can be considered as a good approximation for the timing of the Emad Deh rock avalanche (ca. 5.4 ka), considering that its emplacement should have occurred soon after the deposition of the underlying alluvium in an active floodplain.

### 5.4. The nested secondary landslides

Following the deposition of the Emad Deh rock avalanche, the marls with intercalated limestone beds of the Pabdeh Formation exposed in the scar and affected by sudden unloading, were affected by four landslides (L2-L5 in Fig. 5). The deposits of these landslides are confined between the lateral edges of the scar and the lateral levees of the Emad Deh rock avalanche. Their relative chronology can be inferred on the basis of their cartographic relationships (i.e., superposition, cross-cutting), showing a general eastward migration of the failures. The oldest nested landslide deposit (L2) is 2650 m long, 2030 m wide, covers 4.9 $km^2$, and has a volume of around 45 $Mm^3$. This flow-type landslide displays: (1) well-defined lateral levees; (2) a prominent distal zone with sinuous transverse compressional ridges; and (3) a lobate front with a steep slope around 20 m high below the brink line. The right lateral levee comprises three segments that overlap and extend progressively downslope from the inside of each other in a telescoped left-stepping arrangement. A similar pattern was documented in the North Long John rock avalanche in California by Blair (1999). The inner part of the deposits shows a thick accumulation of the east sector and a courtyard in the western sector. This initially enclosed depression has been opened by a channel breached across the frontal ridge. This landslide can be interpreted as mud-rich and relatively cohesive rock avalanche derived from a planar rockslide on the Pabdeh Formation.

Landslide L3 overlaps landslide L2 and is cross-cut by landslide L4. This is a highly degraded and dissected landslide deposit mostly consisting of easily erodible marls of the Pabdeh Formation. The landslide deposit covers 1.5 $km^2$, reaches 1750 m and 1400 m in length and width, respectively, and has an estimated volume of 12 $Mm^3$. This is interpreted as a short runout planar slide of marl-dominated strata that experienced rapid loss of coherence, and which displacement was partially impeded by landslide L2. Landslide L4 overlaps landslide L2 and cross cuts landslide L3. This is a lobe-shaped deposit with a continuous ridge along the flanks and the frontal snout. The inner sector displays a courtyard with post-landslide deposits that has been opened by a channel breached across the western ridge. The landslide covers around 1 $km^2$, is 1550 m and 1125 m long and wide, respectively, and has an estimated volume of 15 $Mm^3$. This mass movement is interpreted as a rockslide avalanche of Pabdeh limestone and marls derived from the eastern sector of the scar, which runout was restricted by the restraining effect of landslide L2. Landslide L5 overlaps landslide L4 and partially fills the courtyard of the latter. This is a downward widening spatulate lobe 1400 m and 700 m long and width, respectively, covering around 0.6 $km^2$ and with an estimated volume of 12 $Mm^3$. It is interpreted as a slide-flow of marl-dominated Pabdeh initiated as a planar failure. Like landslide L3, the considerable degree of morphological degradation and dissection is attributed to the highly erodible nature of the deposit dominated by marls.

## 6. Other landslides associated with the buried salt dome

The Emad Deh rock avalanche forms part of a spatial cluster of large landslides. Just south of the scar of the Emad Deh landslide complex, in the drainage basin that feeds the eastern alluvial fan, a failure on Pabdeh marls with interbedded limestones has produced a 2 km long slide-flow with a runup on the opposite slope of around 20 m (labelled as L0 in Fig. 5). This landslide has blocked the drainage, forming a landslide dam and an enclosed depression with an ephemeral lake upstream (Fig. 5). Large landslides have also been mapped in the over-steepened slopes at the southeastern sector of the Gavbast Dome related to a rising buried salt diapir. Two of them 4.5 and 2 km long occur associated with the outcrop of the Bangestan Group in the SE sector of the dome (Fig. 4). East of Lavarmistan village, the dip slopes underlain by Pabdeh marls with limestone have produced two long-runout landslides, here designated as Lavarmistan W and E. In this sector the slopes and the dip of the strata are clearly affected by the cumulative over-steepening effect related to the growth of both the Gabvast Anticline and the Gavbast Dome (Fig. 3). Lavarmistan W landslide is a marl-dominated slide-flow 3900 m long, 1150 m wide and with an area of 2.9 $km^2$. A volume of 59 $Mm^3$ has been estimated for this landslide deposit, which displays a pristine distal lobe with steep frontal slopes superimposed on the alluvial fans of the piedmont. Lavarmistan E landslide, 9.4 $km^2$ in area, is 4750 m long and 4125 m wide, and has an approximate volume of 260 $Mm^3$. Two different sectors can be differentiated on the basis of the geomorphic features suggesting that it corresponds to a landslide complex generated by two events: (1) an older eastern sector with rounded and dissected topography; and (2) a younger western sector with pristine flow bands and longitudinal enclosed depressions. This landslide travelled across the piedmont area and surmounted a ridge at least 50 m high on the opposite side of the valley underlain by Bakhtyari conglomerates (Fig. 4). The blocked W-directed drainage eventually breached a narrow and deeply entrenched channel across the landslide dam. The abrupt constriction of the valley at the eastern side of the landslide has been used to build a small dam.

## 7. Discussion

### 7.1. Predisposing, preparatory and triggering factors

The factors that control the development of slope movements can be grouped into four categories: predisposing, preparatory, triggering and sustaining (Glade and Crozier, 2005). Predisposing factors refer to static, inherent characteristics of the slopes that favor their instability. The 420 $Mm^3$ Emad Deh rock avalanche was initiated as a planar rockslide on a high-relief (850 m) dip slope in which a number of predisposing stratigraphic and structural features concur. The stratigraphic succession involved in the slope failure includes the thick (ca. 180 m) and resistant Asmari Limestone, underlain by weak marls with limestone intercalations of the Pabdeh Formation, plus low permeability units (Gachsaran, Mishan) in the lower part of the slope. Stratigraphic successions with units of contrasting mechanical strength on dip slopes

have been proved to be particularly prone to the development of large, long run-out landslides worldwide (e.g., Korup et al., 2013) and in the Zagros Mountains, including the 44,000 $Mm^3$ Seymareh rock avalanche, considered to be the largest exposed landslide on Earth (Roberts, 2008; Roberts and Evans, 2013; Shoaei, 2014; Delchiaro et al., 2019). Ghazipour and Simpson (2017) produced a cartographic inventory of 335 landslides in the Zagros, with volumes ranging between $10^4$ and $3{\cdot}10^{10}$ $m^3$, and analyzed their frequency-size (volume) distribution. The comparison with other inventories worldwide revealed that the Zagros landslides are relatively larger. They attributed this deviation to the frequent occurrence of deep-seated failures in mechanically weak Pabdeh marls overlain by thick and competent Asmari limestones. A principal component analysis revealed a clear correlation between the spatial distribution of large landslides in the Zagros and that of the outcrops of carbonate formations. In the case of the Seymareh rock avalanche, initiated as a planar failure developed on marl and shale units with limestone intercalations (Gurpi and Pabdeh) capped by a carapace of Asmari Limestone, Roberts (2008) and Roberts and Evans (2013) suggested that elevated fluid pressures associated with units of contrasting permeability played a significant destabilizing role. In the analyzed slope, high fluid pressure conditions could temporarily occur at the foot of the slope, where the aquifer of the fractured and karstified Asmari Limestone is confined by the low-permeability Gachsaran and Mishan formations (Fig. 5), although its potential contribution to the instability remains uncertain.

The basal sliding surface of the Emad Deh rockslide-avalanche, as well as those of the subsequent landslides, were controlled by limestone layers interbedded within the upper part of the Pabdeh Formation (Fig. 7A, B). These beds deposited in a marine environment are characterized, in addition to a high dip of 35–40° in the slope, by extensive lateral continuity, extremely planar stratification planes, and bedding-parallel shear surfaces related to active folding, which can reduce the shear strength to residual values in the dip direction. The numerous flexural-slip fault scarps rupturing Quaternary alluvial fans mapped in the area provide factual evidence for the ongoing activity of the flexural folding mechanism (Fig. 3). Bedding-parallel shear commonly occurs along bedding planes that separate units with contrasting stiffness (e.g., limestone-marl; Davies, 1984), eventually controlling the position of slope failures (e.g., Hermanns and Longva, 2012; Gutiérrez et al., 2015). The rock slab could be detached from the slope taking advantage of favorable topographic and structural features: (1) bedding planes daylight at the back (antidip or anaclinal) slope carved in the breached anticline; (2) subvertical fold-normal joints facilitate lateral release; (3) break-out planes across bedding could be formed at the toe of the slope taking advantage of bedding-normal and fold-parallel joints. Both transverse and longitudinal joints are clearly observable in Gavbast Anticline, as is commonly the case in the fracture patterns of the Zagros folds (Stephenson et al., 2007).

Preparatory factors refer to dynamic changes that may shift a slope from a stable to a marginally stable state, without initiating the movement. An instrumental long-term process that contributes to reduce the stability of the slopes in the Zagros Mountain Belt is the continuous creation of topographic relief related to the ongoing collision between the Arabian and Eurasian plates (Fig. 1). Relief rejuvenation in the investigated area is related to the growth of the Gavbast Anticline and the inflation of the Gavbast Dome caused by the rise of a buried diapir of Hormuz salt (Fig. 4). Active fold growth is proved by the presence of bedding-parallel flexural-slip faults that rupture Quaternary alluvial fans (Fig. 3). Moreover, the squeezing of the salt stock by folding is the main driver for the salt rise and the upward bulging of the dome (Jahani et al., 2009). These processes increase the local relief, and over-steepen the gradient of the slopes and the dip of the strata. Gutiérrez et al. (2019) reviews case studies in which relief rejuvenation induced by salt flow leads to the development of landslides. A minimum differential displacement rate of 0.4–0.7 mm/yr has been estimated for the Gavbast anticlinal ridge assuming that the topographic growth of the folds started at ca. 3–2 Ma. This temporal range also indicate a rotation rate for the strata, currently dipping ca. 40°, of around 2°/100 ka. The minimum uplift rate estimated for the crest of Gavbast Dome amounts 0.4–0.6 mm/yr. Slope over-steepening related to the growth of Gavbast Anticline clearly has a long-term impact on all the landslides of the area developed on dip slopes. The influence of the inflation of Gavbast Dome on the Emad Deh rock avalanche, located at the edge of the structure, is uncertain, whereas other landslides undoubtedly occur on slopes rejuvenated by active diapirism (e.g., Lavarmistan E and W) (Fig. 4). An additional preparatory factor for the multiple landslides (L2-L5) developed in the scar created by the Emad Deh rock avalanche is the debuttressing of the suddenly exposed and mechanically weak Pabdeh Formation, previously sustained by a competent carapace of Asmari Limestone (e.g., Korup et al., 2013). Rock mass creep may have also contributed to progressively reduce the stability of the slope, as substantiated for the Seymareh rock avalanche by Delchiaro et al. (2019).

Triggering factors are those that effectively induce the initiation of the movement, shifting the slope from marginally stable to unstable. The most common triggers for large rock avalanches in non-volcanic areas include large earthquakes, slope undermining, and heavy rainstorms (Hewitt et al., 2008; Korup et al., 2013). Erosion at the toe of the slope can be ruled out for the Emad Deh rock avalanche considering its geomorphic setting, and severe precipitation seems very unlikely in this arid area with relatively large outcrops of rocks with a high infiltration capacity (i.e., fractured and karstified limestone). The most reasonable trigger is a large $M_w \geq 6.5$–7 paleoearthquake (e.g., Keefer, 1999) occurred at ca. 5.4 ka. This hypothesis is supported by the fact that the Emad Deh rock avalanche forms part of a spatial cluster of large bedrock landslides, including two similar-size gigantic slope failures and evidence of recurrent instability (Strom, 2015). Back analyses, such as stress-strain numerical modelling that take into consideration the potential elasto-plastic behavior of the rock mass would provide deeper insight into this untested hypothesis. The putative earthquake was likely sourced from a blind N-dipping reverse fault located beneath the Gavbast Anticline. Such structure could correspond to a normal fault created during the Permo-Triassic rifting and inverted in the current compressional regime. An alternative is the Mountain Front Fault inferred by Berberian (1995), but this structure, around 40 km to the south, is not associated with a asymmetric anticline in this sector (e.g. Gezeh Anticline), but to the southern limit of exposure of the Asmari Limestone (Fig. 3). According to the historical and instrumental earthquake catalogues, the area has been struck by several M 5.5–6.2 earthquakes, but none of them has triggered any major landslide (Berberian, 2014) (Fig. 3). Interestingly, reverse fault earthquakes of $M_w \geq 6.7$ in the Fars Arc (1972 Ghir, and 1977 Khurgu; Dewey and Grantz, 1973; Berberian and Papastamatiou, 1978) typically occur associated with anomalous anticlines characterized by: (1) asymmetric geometry with steeper southern limbs; (2) significant down-to-the-south topographic steps and stratigraphic throws, and (3) rare exposures of old formations (Berberian, 1995; Nissen et al., 2011). Nissen et al. (2011) suggest that these folds geometrically distinct from the typical symmetric folds of the Simply Folded Belt, indicate the location of major blind reverse faults capable of producing large Mw ~7 earthquakes. Gavbast Anticline meets all these conditions (Fig. 3), in addition that it controls the main watershed divides of the Fars Arc (Fig. 2), suggesting that is underlain by a major basement reverse fault. According to the empirical relationships of Wells and Coppersmith (1994), $M_w$ 7 reverse fault earthquakes require rupture lengths of around 45 km, which is compatible with the >100 km length of Gavbast Anticline. The triggering of the gigantic Seymareh rock avalanche, sourced from the limb of the most prominent growing anticline in the Lurestan Arc, has been tentatively attributed to a large paleoearthquake occurred at ca. 10 ka (Roberts, 2008; Roberts and Evans, 2013; Shoaei, 2014; Delchiaro et al., 2019). The potential seismic trigger has been supported by pseudostatic and dynamic back analyses, indicating the need for prolonged low-frequency ground shaking typical of earthquakes with magnitudes exceeding 7 (Fomenko

et al., 2021). Coseismic strong ground motion causes cyclic changes in the stresses acting on hillslopes and can reduce the strength of the materials. Ground motion can be significantly amplified due to site effects, including the presence of weak geological materials (i.e., low elastic modulus) and topographic ridges, where constructive interference of seismic waves projected upwards causes increasing amplifications towards the ridge crest. The presence beneath Gavbast Dome of a wide "pipe" around 10 km in vertical dimension filled with extremely weak salt may have contributed to amplify the strong ground motion in its vicinity. Moreover, data from historical thrust fault earthquakes indicate that slope failures preferentially occur in the hanging wall of the seismogenic fault and on hillslopes facing away from the earthquake source (Meunier et al., 2007; Wang et al., 2007; Hovious and Meunier, 2012; Khan et al., 2020), as would be the case of the Emad Deh rock avalanche if it was triggered by an earthquake sourced from a reverse fault.

### 7.2. Reconstruction of the rock avalanche depositional history

The variable morphological features of the rock avalanche deposit and its spatial relationships with the geomorphic context allow deriving some inferences about its depositional history (Fig. 5). The detachment of the rock slab, with its basal failure situated in the upper part of the Pabdeh Formation, was probably triggered by topographically-amplified ground motion related to a large earthquake at ca. 5.4 ka. The rockslide underwent rapid disintegration, fragmentation and expansion from the initial part of its travel path, as supported by the characteristics of the deposits at their proximal edge, situated at the foot of the mountain front: (1) angular breccia with a carapace of large boulders; and (2) outward offset of the lateral levees with respect to the flanks of the scar. In the proximal sector of the piedmont the stream of rock fragments travelled on relatively steep coalescing alluvial fans, with an older and higher fan surface on the east side. The alluvial fan deposits with a high proportion of limestone and gypsum particles and under arid conditions are rapidly hardened by precipitation of secondary carbonate. The rock avalanche path was to some extent conditioned by the presence of an interfan trough and the higher lateral confinement imposed by the more prominent eastern fan (e.g., Blair, 1999), as indicated by the slight westward deviation of its medial axis with respect to the dip direction of the "detachment ramp" at the source. The relatively high basal and lateral friction in this proximal alluvial fan environment prompted the accumulation of a significant volume of deposits filling the interfan trough, plus the large lateral levees sheared off form the main stream of rock fragments (Fig. 5). The rock avalanche experienced a sharp change in its depositional behavior when it reached the flat floodplain surface underlain by soft alluvium. Geomorphic evidence for this change is provided by the sharp distal edge of the proximal deposits, defined by a rectilinear downslope-facing scarp (Fig. 7D), plus the adjacent intermediate depression with very limited accumulation of deposits (Fig. 5). This spatial variation suggests that the rock avalanche did not experienced any significant flow dissipation in this section due to low basal friction, and had sufficient power to transport most of the material. It is not known whether the floodplain deposits were liquefied by the sudden loading exerted by the rock avalanche. Further downflow, the rock avalanche underwent substantial radial spreading, with the consequent increase in the basal friction area and the thinning of the flow, leading to accumulation of deposits compartmentalized into flat-topped polygonal hills and more distally into compound and single conical hills, often radially aligned (Figs. 9, 10). The conical hills can be envisioned as patchy accumulations with its morphology determined by the repose angle of the material. The variable morphological pattern observed in the distal sector can be attributed to the longitudinal and transverse breakup of the radially spreading and thinning debris stream (i.e., extensional flow) (Dufresne and Davies, 2009). According to Dufresne and Davies (2009) the formation of radially aligned ridges and hummocks is favored by weakly cohesive avalanches moving on soft substrate.

### 7.3. Rock avalanche mobility

The Emad Deh rock avalanche displays a very long runout, despite it experienced significant spreading (expansion factor of 2.3) in the unconfined piedmont. The maximal height drop (H) of 914 m and the runout (L) of 9280 m yield a H/L mobility index (*fahrböschung*, or apparent coefficient of friction; Heim, 1932; Scheidegger, 1973) of 0.09, and a travel angle of 5.6°. The position of the Emad Deh rock avalanche in the H/L vs. volume plot produced by Aaron and McDougall (2019) with databases of case studies worldwide reveals its extraordinary mobility (Fig. 11). The H/L index is comparable with that of the Sherman Glacier rock avalanche, triggered by the great 1964 Alaska earthquake and deposited on ice (McSaveney, 1978), or close to the extraordinary Seymareh rock avalanche (Zagros Mountains, Iran), with an exceptional H/L ratio (1210 m/19,000 m) of 0.06, and a travel angle of 3.6°, despite is partial frontal confinement (Roberts and Evans, 2013). Strom et al. (2019), using an inventory of around 600 rock avalanches from Central Asia, produced regressions for the quantitative characterization of their mobility, differentiating between confined and unconfined settings, a factor that may have a strong impact on runout (i.e., lateral spreading, frontal obstruction). They obtained higher coefficients of determinations with parameters other than the frequently used H/L index, such as the product VxHmax (volume at the source and maximal vertical drop), which is a first approximation to the energy released by the slope failure. Their regression between L (runout) and the product VxHmax for unconfined rock avalanches predicts for the Emad Deh rock avalanche (V: 350 $Mm^3$ and Hmax: 914 m) a runout of 4.9 km, which is almost half of that experienced by the avalanche (9.3 Km), highlighting its anomalously high mobility.

A wide variety of mechanisms have been proposed to explain the surprisingly long runout of large ($>10^6$ $m^3$) rock avalanches (Legros, 2002; Hungr, 2006; Davies and McSaveney, 2012): (1) Dynamic rock fragmentation, whereby the breakage of rock particles under high normal stress is accompanied by the release of elastic energy previous stored in the rock (Davies and McSaveney, 1999, 2002, 2012, Pollet and Schneider, 2004). The energy released within the confined granular flow is radiated as acoustic emissions producing a vibration that generates an interstitial pressure reducing inter-particle stresses. Davies and McSaveney (2012) point that this process can work in every circumstance given the universal association of long runout rock avalanches with intense rock crushing. Some authors claim that rock fragmentation is an energy-consuming process (Hungr, 2006). (2) Lubrication by a water-saturated soil substrate liquefied by undrained loading, eventually accompanied by entrainment of soft soil in the landslide path (Hungr and Evans, 2004; Hungr, 2006). Davies and McSaveney (2012) claim that this is not an indispensable mechanism, since rock avalanches occur on every kind of substrate (bedrock, soil, ice). Some authors also consider that bulldozing material from the substrate is an energy-consuming process. (3) Mechanical fluidization postulates that interactions among rapidly moving particles, especially in the basal region, generates a dispersive pressure that maintains them away from each other (dilated) reducing the internal resistance to shear stress (Davies, 1982). (4) Acoustic fluidization, whereby vibrational energy arises in non-fragmenting granular shear flows from lateral velocity components related to particle interactions (Melosh, 1979; Collins and Melosh, 2003; Johnson and Campbell, 2017). (5) Basal sliding on dissociated or melted rock (Erismann, 1979; Masch et al., 1985; De Blasio and Elverhøi, 2008; Hu et al., 2019), which seems to operate in few cases (Davies and McSaveney, 2012). (6) Vertical oscillations in quasi-rigid plugs of rock avalanche material that reduce the contact time with the underlying ground (Cagnoli and Quareni, 2009). (7) Lubrication by a cushion of trapped and compressed air (Shreve, 1968). (8) Fluidization by air-extrusion that maintains particles in a dilated state (Kent, 1966). (9) Fluidization by escaping water vapor derived from the vaporization of groundwater by frictional heating (Goguel, 1978). (10) Vibration of the moving mass by seismic shaking (McSaveney, 1978;

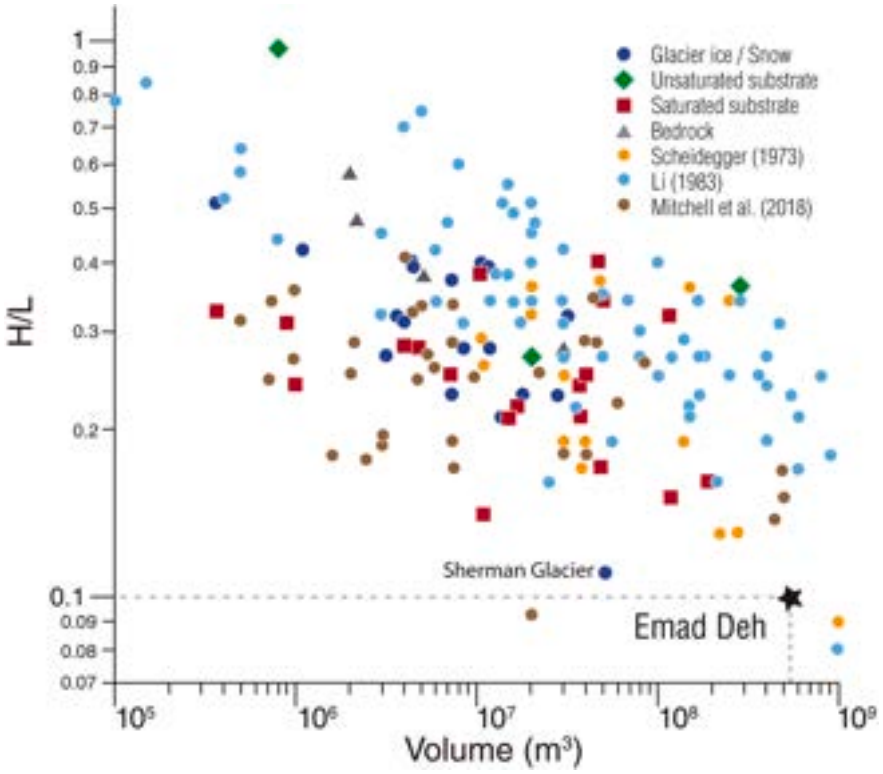


**Fig. 11.** Plot of volume versus H/L ratio of rock avalanches from multiple databases, including data of Aaron and McDougall (2019) that differentiate the type of substrate. The graph illustrates the large dispersion of the data, a general trend of higher mobility with increasing volume (size effect), and the extraordinary large runout of the Emad Deh rock avalanche. Adapted from Aaron and McDougall (2019).

Hazlett et al., 1991). The two most widely accepted hypotheses are those related to the fragmentation process (dynamic rock fragmentation), supported by the omnipresent shattered breccias found in rock avalanche deposits, and basal lubrication by a liquefied soil substrate. The extraordinarily high mobility of the Emad Deh rock avalanche is probably related to the combined effect of both mechanisms. Basal lubrication, supported by soft-sediment deformation observed beneath the rock avalanche (Fig. 8c), most probably played a role along 70 % of the flow path, beyond the coalescing alluvial fans (Fig. 5).

## 8. Conclusions

The ca. 420 $Mm^3$ Emad Deh rock avalanche was initiated as a rockslide at the northern limb of the growing Gavbast Anticline and around the edge of the inflating Gavbast Dome, related to a buried salt diapir. The collapsed rock slab comprised marls with limestone intercalations of the Padbeh Formation, overlain by a thick and competent caprock of Asmari Limestone. The unconfined rock avalanche deposit, covering 31,6 $km^2$, was accumulated on coalescing alluvial fans and floodplain deposits. Three main sectors with distinctive morphological features attributable to variable flow-depositional behavior have been differentiated: (A) a proximal area showing a continuous breccia with an abrupt distal termination and flanked by paired lateral levees; (B) an intermediate depression with very limited deposition; and (C) a distal sector with substantial spreading featured by flat-topped polygonal hills and radially aligned and progressively smaller conical hills. In the proximal sector, the path of the avalanche was slightly deflected to the west by the presence of a higher fan on the eastern side, and the deposits filled an interfan trough. The abrupt variation in the morpho-sedimentary style observed between the proximal and the intermediate sector is attributed to a change in substrate, from relatively indurated alluvial fan deposits to soft and probably saturated floodplain sediments. The polygonal and conical hills of the distal sector record the breakup of the debris stream by radial spreading under extensional flow conditions. Sometime after the Emed Deh rock failure, four large landslides (45–12 $Mm^3$) occurred in the debuttressed and suddenly unloaded scar created by the former slope failure. The resulting landslide deposits derived from Pabdeh marls and limestone were confined and nested between the flanking wall of the scar and the lateral levees of the Emad Deh rock avalanche.

The sudden N-directed loading induced by the emplacement of the rock avalanche on the soft fluvial deposits underlying the floodplain led to the formation of N-verging folds in the alluvium. An OSL age of 5.4 ± 0.3 ka obtained from a silt bed in the folded fluvial sequence situated 1.1 m below the base of the rock avalanche deposit provides a good approximation for the age of the latter.

The predisposing factors that favored the formation of the Emad Deh rockslide-avalanche include the high-relief, a stratigraphic succession of competent limestone underlain weak marls, limestone beds in the failure zone with extremely planar stratification planes, large lateral continuity, and reduced shear strength by active flexurtal folding, and joints with favorable orientation for the release of the rock slab.

The main preparatory factor was relief rejuvenation by the growth of the Gavbast Anticline (>0.4–0.7 mm/yr) and probably also the inflation of the Gavbast Dome (>0.4–0.6 mm/yr) related to the rise of the buried salt diapir. Slope and dip over-steepening by diapiric activity have clearly played some role in the development of other large landslides located within the Gavbast Dome, including the 240 $Mm^3$ Lavarmistan E rock avalanche.

The Emad Deh rock avalanche was likely triggered by a $M_w \geq 6.5$–7 paleoearthquake at ca. 5.4 ka. The source of this event was probably a N-dipping blind reverse fault situated beneath the asymmetric Gavbast Anticline.

The notorious gap that shows paleoearthquake data in the Zagros Fold-and-Thrust Belt could be partially filled by identifying and dating secondary paleoseismic evidence, such as coseismic landslides and

displacement events on flexural-slip fault scarps that may record the episodic growth of folds underlain by blind seismogenic reverse faults. This information would allow expanding the earthquake catalog, constructing more comprehensive seismic source models and producing more reliable seismic hazard estimates. A twofold major challenge is faced; unequivocally demonstrating the coseismic nature of specific large landslides and dating them.

Supplementary data to this article can be found online at https://doi.org/10.1016/j.geomorph.2022.108527.

## Declaration of competing interest

The authors declare the following financial interests/personal relationships which may be considered as potential competing interests:

Francisco Gutierrez reports financial support was provided by Spain Ministry of Science and Innovation. Francisco Gutierrez reports equipment, drugs, or supplies was provided by German Aerospace Center DLR.

## Data availability

Data will be made available on request.

## Acknowledgements

The authors are very grateful to the major of Gavbast village, Mohammad Chubaki for providing logistic support, and to Tomas Panek and Michele Delchiaro for their insightful reviews. Edwin Nissen and Ezgi Karasözen kindly provided data from their relocated earthquake catalog of the Fars Arc. The work by FG was supported by a Salvador de Madariaga grant (PR19/00028) and projects (CGL2017-85045-P, DIAPERNO: PID2021-123189NB-I00) of the Spanish Government (Ministerio de Ciencia e Innovación). The TanDEM-X digital elevation models were provided by the German Aerospace Center (grant DEM_GEOL288).

## References

Aaron, J., McDougall, S., 2019. Rock avalanche mobility: the role of path material. Eng. Geol. 257, 105126.
Authemayou, C., Bellier, O., Chardon, D., Benedetti, L., Malekzade, Z., Claude, C., Angeletti, B., Shabanian, E., Abbassi, M.R., 2009. Quaternary slip-rates of the Kazerun and the Main recent Faults: active strike-slip partitioning in the Zagros fold-and-thrust belt. Geophys. J. Int. 178, 524–540.
Bagnold, R.A., 1954. Experiments on a gravity-free dispersion of large solid spheres in a Newtonian fluid under shear. Proceedings of the Royal Society of London. Series A. Mathematic. Phys. Sci. 225 (1160), 49–63.
Barnhart, W.D., Lohman, R.B., Mellors, R.J., 2013. Active accommodation of plate convergence in Southern Iran: earthquake locations, triggered aseismic slip, and regional strain rates. J. Geophys. Res. Solid Earth 118, 5699–5711.
Berberian, M., 1995. Master "blind" thrust faults hidden under the Zagros folds: active basement tectonics and surface morphotectonics. Tectonophysics 241, 193–224.
Berberian, M., 2014. Earthquakes and Coseismic Surface Faulting on the Iranian Plateau. Elsevier, Amsterdam.
Berberian, M., Papastamatiou, D., 1978. Khurgu (North Bandar Abbas, Iran) earthquake of March 21, 1977: a preliminary field report and seismotectonic discussion. Bull. Seismol. Soc. Am. 68, 411–428.
Blair, T.C., 1999. Form, facies, and depositional history of the North Long John rock avalanche, Owens Valley, California. Can. J. Earth Sci. 36, 855–870.
Blanc, E.P., Allen, M.B., Inger, S., Hassani, H., 2003. Structural styles in the Zagros simple folded zone, Iran. Journal of the Geological Society 160, 401–412.
Brettis, B., Bartl, N., Grasemann, B., 2011. Lateral fold growth and linkage in the Zagros fold and thrust belt (Kurdistan, NE Iraq). Basin Res. 223, 615–630.
Burberry, C.M., Cosgrove, J.W., Liu, J.G., 2008. Spatial arrangement of fold types in the Zagros simply Folded Belt, Iran, indicated by landform morphology and drainage pattern characteristics. J. Maps 4, 417–430.
Burberry, C.M., Cosgrove, J.W., Liu, J.G., 2010. A study of fold characteristics and deformation style using the evolution of the land surface: Zagros Simply Folded Belt, Iran. Geol. Soc. Lond. Spec. Publ. 330, 139–154.
Cagnoli, B., Quareni, F., 2009. Oscillation-induced mobility of flows of rock fragments with quasi-rigid plugs in rectangular channels with frictional walls: a hypothesis. Eng. Geol. 103, 23–32.
Callot, J.P., Jahani, S., Letouzey, J., 2007. The role of pre-existing diapirs in fold and thrust belt development. In: Lacombe, O., Roure, F., Lavé, J., Vergés, J. (Eds.), Thrust Belts and Foreland Basins. Springer, Berlin, pp. 1–17.
Clark, P.J., Evans, F.C., 1954. Distance to nearest neighbor as a measure of spatial relationships in populations. Ecology 35, 445–453.
Collignon, M., Yamato, P., Castelltort, S., Kaus, B.J., 2016. Modeling of wind gap formation and development of sedimentary basins during fold growth: application to the Zagros Fold Belt, Iran. Earth Surf. Process. Landforms 41, 1521–1535.
Collins, G.S., Melosh, H.J., 2003. Acoustic fluidization and the extraordinary mobility of sturzstroms. J. Geophys. Res. Solid Earth 108, 2473.
Davies, G.H., 1984. Structural Geology of Rocks and Regions. John Wiley & Sons, New York.
Davies, T.R., 1982. Spreading of rock avalanche debris by mechanical fluidization. Rock Mech. 15, 9–24.
Davies, T.R., McSaveney, M.J., 1999. Runout of dry granular avalanches. Can. Geotech. J. 36, 313–320.
Davies, T.R., McSaveney, M.J., 2002. Dynamic simulation of the motion of fragmenting rock avalanches. Can. Geotech. J. 39, 789–798.
Davies, T., McSaveney, M., 2012. Mobility of long-runout rock avalanches. In: Clague, J. J., Stead, D. (Eds.), Landslides: Types, Mechanisms and Modeling. Cambridge University Press, Cambridge, pp. 50–58.
De Blasio, F.V., Elverhøi, A., 2008. A model for frictional melt production beneath large rock avalanches. J. Geophys. Res. Earth Surf. 113, F02014.
Delchiaro, M., Iacobucci, G., Troiani, F., Della Seta, M., Ballato, P., Aldega, L., 2022. Morphoevolution of the Seymareh landslide-dam lake system (Zagros Mountains, Iran): Implications for Holocene climate and environmental changes. Geomorphology 413, 108367.
De Waele, J., Gutiérrez, F., 2002. Karst Hydrogeology, Geomorphology and Caves. Wiley, Chichester.
Delchiaro, M., Della Seta, M., Martino, S., Dehbozorgi, M., Nozaem, R., 2019. Reconstruction of river valley evolution before and after the emplacement of the giant Seymareh rock avalanche (Zagros Mts., Iran). Earth Surf. Dyn. 7, 929–947.
Dewey, J.W., Grantz, A., 1973. The Ghir earthquake of April 10, 1972 in the Zagros Mountains of southern Iran: seismotectonic aspects and some results of a field reconnaissance. Bull. Seismol. Soc. Am. 63, 2071–2090.
Dufresne, A., Bösmeier, A., Prager, C., 2016. Sedimentology of rock avalanche deposits. Case study and review. Earth Sci. Rev. 163, 234–259.
Dufresne, A., Davies, T.R., 2009. Longitudinal ridges in mass movement deposits. Geomorphology 105, 171–181.
Durcan, J., King, G., Duller, G.A.T., 2015. DRAC: dose rate and age calculator for trapped charge dating. Quat. Geochronol. 28, 54–61.
Evans, S.G., Bishop, N.F., Smoll, L.F., Murillo, P.V., Delaney, K.B., Oliver-Smith, A., 2009. A re-examination of the mechanism and human impact of catastrophic mass flows originating on Nevado Huascarán, Cordillera Blanca, Peru in 1962 and 1970. Eng. Geol. 108, 96–118.
Erismann, T.H., 1979. Mechanisms of large landslides. Rock Mechanics 12, 15–46.
Fakhari, M.D., Axen, G.J., Horton, B.K., Hassanzadeh, J., Amini, A., 2008. Revised age of proximal deposits in the Zagros foreland basin and implications for Cenozoic evolution of the High Zagros. Tectonophysics 451, 170–185.
Fomenko, I.K., Nikiforov, S.P., Shoaei, Z., Strom, A.L., Tarabukin, V.V., Zerkal, O.V., 2021. Justification of seismic triggering of large prehistoric rockslides in Zagros (Iran) and Greater Caucasus (Russia). IOP Conf. Ser. Earth Environ. Sci. 833, 012169.
Galbraith, R.F., Roberts, R.G., Laslett, G.M., Yoshida, H., Olley, J.M., 1999. Optical dating of single and multiple grains of quartz from Jinmium Rock Shelter, Northern Australia: part I, experimental design and statistical models. Archaeometry 41, 339–364.
Ghazipour, N., Simpson, G., 2017. Size distribution and controls of landslides in the Zagros mountain belt (Iran). Tectonic evolution, collision, and seismicity of Southwest Asia. In: Sorkhabi, E. (Ed.), Tectonic Evolution, Collision and Seismicity of Southwest Asia. In Honor of Manuel Berberian's Forty-Five Years of Research Contributions, 525. The Geological Society of America Special Paper, pp. 1–21.
Glade, T., Crozier, M.J., 2005. The nature of landslide hazard impact. In: Glade, T., Anderson, M., Crozier, M. (Eds.), Landslide Hazard and Risk. Wiley, Chichester, pp. 43–74.
Goguel, J., 1978. Scale-dependent rockslide mechanisms, with emphasis on the role of pore fluid vaporization. In: Voight, B. (Ed.), Rock Slides and Avalanches. Developments in Geotechnical Engineering, 1. Elsevier, Amsterdam, pp. 693–705.
Goorabi, A., 2020. Detection of landslide induced by large earthquake using InSAR coherence techniques–Northwest Zagros, Iran. Egypt. J. Remote Sens. Space Sci. 23, 195–205.
Guerin, G., Mercier, N., Adamiec, G., 2011. Dose-rate conversion factors: update. Ancient TL 29, 5–8.
Gutiérrez, F., Carbonel, D., Kirkham, R.M., Guerrero, J., Lucha, P., Matthews, V., 2014. Can flexural-slip faults related to evaporite dissolution generate hazardous earthquakes? The case of the Grand Hogback Monocline of west-central Colorado. GSA Bull. 126, 1481–1494.
Gutiérrez, F., Linares, R., Roqué, C., Zarroca, M., Carbonel, D., Rosell, J., Gutiérrez, M., 2015. Large landslides associated with a diapiric fold in Canelles Reservoir (Spanish pyrenees): detailed geological–geomorphological mapping, trenching and electrical resistivity imaging. Geomorphology 241, 224–242.
Gutiérrez, F., Sevil, J., Silva, P.G., Roca, E., Escosa, F., 2019. Geomorphic and stratigraphic evidence of Quaternary diapiric activity enhanced by fluvial incision. Navarrés salt wall and graben system, SE Spain. Geomorphology 342, 176–195.
Harrison, J.V., 1930. The geology of some salt-plugs in Laristan, southern Persia. Q. J. Geol. Soc. 86, 463–522.
Harp, E.L., Crone, A.J., 2006. Landslides triggered by the October 8, 2005, Pakistan earthquake and associated landslide-dammed reservoirs. In: US Geological Survey Open-file Report 2006-1052, 13 p.

Hazlett, R.W., Buesch, D., Anderson, J.L., Elan, R., Scandone, R., 1991. Geology, failure conditions, and implications of seismogenic avalanches of the 1944 eruption at Vesuvius, Italy. J. Volcanol. Geotherm. Res. 47, 249–264.
Heim, A., 1932. Landslides and Human Lives. Bi-Tech Publishers, Vancouver.
Hermanns, R.L., Longva, O., 2012. Rapid rock-slope failures. In: Clague, J.J., Stead, D. (Eds.), Landslides: Types, Mechanisms and Modeling. Cambridge University Press, Cambridge, pp. 50–58.
Hessami, K., Koyi, H.A., Talbot, C.J., Tabasi, H., Shabanian, E., 2001. Progressive unconformities within an evolving foreland fold–thrust belt, Zagros Mountains. J. Geol. Soc. 158, 969–981.
Hewitt, K., Clague, J.J., Orwin, J.F., 2008. Legacies of catastrophic rock slope failures in mountain landscapes. Earth Sci. Rev. 87, 1–38.
Homke, S., Vergés, J., Garcés, M., Emami, H., Karpuz, R., 2004. Magnetostratigraphy of Miocene-Pliocene Zagros foreland deposits in the front of the Push-e Kush arc (Lurestan Province, Iran). Earth Planet. Sci. Lett. 225, 397–410.
Hovious, N., Meunier, P., 2012. Earthquake ground motion and patterns of seismically induced landsling. In: Clague, J.J., Stead, D. (Eds.), Landslides: Types, Mechanisms and Modeling. Cambridge University Press, Cambridge, pp. 24–36.
Hu, W., Huang, R., McSaveney, M., Yao, L., Xu, Q., Feng, M., Zhang, X., 2019. Superheated steam, hot CO2 and dynamic recrystallization from frictional heat jointly lubricated a giant landslide: field and experimental evidence. Earth Planet. Sci. Lett. 510, 85–93.
Hungr, O., 2006. Rock avalanche occurrence, process and modelling. In: Evans, S.G., Scarascia-Mugnozza, G., Strom, A.L., Hermanns, R.L., Ischuk, A., Vinnichenko, S. (Eds.), Landslides From Massive Rock Slope Failure. Springer, Dordrecht, pp. 243–266.
Hungr, O., Evans, S.G., 2004. Entrainment of debris in rock avalanches: an analysis of a long run-out mechanism. Geol. Soc. Am. Bull. 116, 1240–1252.
Jackson, J.A., 1980. Reactivation of basement faults and crustal shortening in orogenic belts. Nature 283, 343–346.
Jackson, M.P.A., Hudec, M.R., 2017. Salt Tectonics. Principles and Practice. Cambridge University Press, Cambridge.
Jahani, S., Callot, J.P., Frizon de Lamotte, D., Letouzey, J., Leturmy, P., 2007. The salt diapirs of the eastern Fars Province (Zagros, Iran): a brief outline of their past and present. In: Lacombe, O., Roure, F., Lavé, J., Vegés, J. (Eds.), Thrust Belts and Foreland Basins. Springer, Berlin, pp. 289–308.
Jahani, S., Callot, J.P., Letouzey, J., Frizon de Lamotte, D., 2009. The eastern termination of the Zagros Fold-and-Thrust Belt, Iran: structures, evolution, and relationships between salt plugs, folding, and faulting. Tectonics 28, TC6004.
Jahani, S., Hassanpour, J., Mohammadi-Firouz, S., Letouzey, J., de Lamotte, D.F., Alavi, S.A., Soleimany, B., 2017. Salt tectonics and tear faulting in the central part of the Zagros Fold-Thrust Belt, Iran. Mar. Petrol. Geol. 86, 426–446.
Jibson, R.W., 2009. Using landslides for paleoseismicanalysis. In: McCalpin, J.P. (Ed.), Paleoseismology. Elsevier, Amsterdam, pp. 565–601.
Jibson, R.W., 2012. Models of the triggering of landslides during earthquakes. In: Clague, J.J., Stead, D. (Eds.), Landslides: Types, Mechanisms and Modeling. Cambridge University Press, Cambridge, pp. 196–206.
Johnson, B.C., Campbell, C.S., 2017. Drop height and volume control the mobility of long-runout landslides on the Earth and Mars. Geophys. Res. Lett. 44, 12–091.
Karasözen, E., Nissen, E., Bergman, E.A., Ghods, A., 2019. Seismotectonics of the Zagros (Iran) from orogen-wide, calibrated earthquake relocations. J. Geophys. Res. Solid Earth 124, 9109–9129.
Keefer, D.K., 1999. Earthquake-induced landslides and their effects on alluvial fans. J. Sediment. Res. 69, 84–104.
Kent, P.E., 1966. The transport mechanism in catastrophic rock falls. J. Geol. 74, 79–83.
Kent, P.E., 1979. The emergent Hormuz salt plugs of southern Iran. J. Pet. Geol. 2, 117–144.
Khadivi, S., Mouthereau, F., Larrasoaña, J.C., Vergés, J., Lacombe, O., Khademi, E., Beamud, E., Melinte-Dobrinescu, M., Suc, J.P., 2010. Magnetochronology of synorogenic Miocene foreland sediments in the Fars arc of the Zagros Folded Belt (SW Iran). Basin Res. 22, 918–932.
Khan, S., van der Meijde, M., van der Werff, H., Shafique, M., 2020. The impact of topography on seismic amplification during the 2005 Kashmir earthquake. Nat. Hazards Earth Syst. Sci. 20, 399–411.
Korup, O., Schneider, D., Huggel, C., Dufresne, A., 2013. Long-runout landslides. In: Marston, R.A., Stoffel, M. (Eds.), Treatise of Geomorphology, Vol. 7. Mountain and Hillslope Geomorphology Academic Press, San Diego, pp. 183–188.
McCalpin, J.P., Gutierrez, F., Bruhn, R.L., Guerrero, J., Pavlis, T.L., Lucha, P., 2020. Tectonic geomorphology and late Quaternary deformation on the Ragged Mountain fault, Yakutat microplate, south coastal Alaska. Geomorphology 351, 106875.
McColl, S.T., Davies, T.R., 2011. Evidence for a rock-avalanche origin for the Hillocks "moraine", Otago, New Zealand. Geomorphology 127, 216–224.
Lagmay, A.M.A., Ong, J.B.T., Fernandez, D.F.D., Lapus, M.R., Rodolfo, R.S., Tengonciang, A.M.P., Soria, J.L.A., Baliatan, E.G., Quimba, Z.L., Uichanco, C.L., Paguican, E.M.R., Remedio, A.R.C., Lorenzo, G.R.H., Avial, F.B., Valdivia, W., 2006. Scientists investigate recent Philippine landslide. EOS Trans. Am. Geophys. Union 87, 121–124.
Lay, T., Kanamori, H., Ammon, C.J., Nettles, M., Ward, S.N., Aster, R.C., Beck, S.L., Bilek, S.L., Brudzinski, M.R., Butler, R., DeShon, H.R., Ekstrom, G., Satake, K., Sipkin, S., Henson, B., 2005. The great Sumatra-Andaman earthquake of 26 December 2004. Science 308, 1127–1133.
Legros, F., 2002. The mobility of long-runout landslides. Eng. Geol. 63, 301–331.
Letouzey, J., Sherkati, S., 2004. Salt Movement, Tectonic Events, and Structural Style in the Central Zagros Fold and Thrust Belt (Iran). In: 24th Annual GCSSEPM Foundation. Bob F. Perkins Research Conference: Salt-Sediment Interactions and Hydrocarbon Prospectivity: Concepts, Applications, and Case Studies for the 21st Century, Gulf Coast Section. Society for Sedimentary Geology, Houston, Texas.
Leturmy, P., Molinaro, M., de Lamotte, D.F., 2010. Structure, timing and morphological signature of hidden reverse basement faults in the Fars Arc of the Zagros (Iran). In: Leturmy, P., Robin, C. (Eds.), Tectonic and Stratigraphic Evolution of Zagros and Makran during the Mesozoic-Cenozoic. Geological Society, 330. Special Publications, London, pp. 121–138.
Lohman, R.B., Simons, M., 2005. Locations of selected small earthquakes in the Zagros mountains. Geochem. Geophys. Geosyst. 6, Q03001.
Macedo, J., Marshak, S., 1999. Controls on the geometry of fold-thrust belt salients. Geol. Soc. Am. Bull. 111, 1808–1822.
Masch, L., Wenk, H.R., Preuss, E., 1985. Electron microscopy study of hyalomylonites—evidence for frictional melting in landslides. Tectonophysics 115, 131–160.
McQuarrie, N., 2004. Crustal scale geometry of the Zagros fold–thrust belt, Iran. Journal of Structural Geology 26, 519–535.
McSaveney, M.J., 1978. Sherman glacier rock avalanche, Alaska, USA. In: Voigt, B. (Ed.), Developments in Geotechnical Engineering, Vol. 14. Elsevier, Amsterdam, pp. 197–258.
Meunier, P., Hovius, N., Haines, A.J., 2007. Regional patterns of earthquake-triggered landslides and their relation to ground motion. Geophys. Res. Lett. 34, L20408.
Molinaro, M., Leturmy, P., Guezou, J.C., Frizon de Lamotte, D., Eshraghi, S.A., 2005. The structure and kinematics of the southeastern Zagros fold-thrust belt, Iran: from thin-skinned to thick-skinned tectonics. Tectonics 24, TC3007.
Melosh, H.J., 1979. Acoustic fluidization: a new geologic process? J. Geophys.Res. Solid Earth 84, 7513–7520.
Motiei, H., 1993. Stratigraphy of Zagros. Geological Survey of Iran, Tehran.
Mouthereau, F., Tensi, J., Bellahsen, N., Lacombe, O., De Boisgrollier, T., Kargar, S., 2007. Tertiary sequence of deformation in a thin-skinned/thick-skinned collision belt: The Zagros Folded Belt (Fars, Iran). Tectonics 26, TC5006.
Nissen, E., Tatar, M., Jackson, J.A., Allen, M.B., 2011. New views on earthquake faulting in the Zagros fold-and-thrust belt of Iran. Geophys. J. Int. 186, 928–944.
Oberlander, T.M., 1985. Origin of drainage transverse to structures in orogens. In: Morisawa, M., Hack, J.T. (Eds.), Tectonic Geomorphology. Allen and Unwin Boston, pp. 155–182.
O'Brien, C.A.E., 1957. Salt diapirism in South Persia. Geol. Mijnb. 19, 357–376.
Plafker, G., Ericksen, G.E., 1978. Nevados Huascaran avalanches, Peru. In: Voigt, B. (Ed.), Developments in Geotechnical Engineering, Vol. 14. Elsevier, Amsterdam, pp. 277–314.
Perry, J.T.O'.B., Setudehnia, A., Nars, M., 1965. South-East Fars Geological Compilation Map at 1:250,000. Iranian Oil Operatin Companies, Geological and Exploration Division, Tehran.
Pollet, N., Schneider, J.L., 2004. Dynamic disintegration processes accompanying transport of the Holocene Flims sturzstrom (Swiss Alps). Earth Planet. Sci. Lett. 221, 433–448.
Prescott, J.R., Hutton, J.T., 1994. Cosmic ray contributions to dose rates for luminescence and ESR dating: large depths and long term time variations. Radiat. Meas. 23, 497–500.
Rajabi, A.M., Mahdavifar, M.R., Khamehchiyan, M., Del Gaudio, V., 2011. A new empirical estimator of coseismic landslide displacement for Zagros Mountain region (Iran). Nat. Hazards 59, 1189–1203.
Ramsey, L.A., Walker, R.T., Jackson, J., 2008. Fold evolution and drainage development in the Zagros mountains of Fars province, SE Iran. Basin Res. 20, 23–48.
Roberts, N.J., 2008. Structural and geologic controls on gigantic (>1 Gm3) landslides in carbonate sequences. In: Case studies from the Zagros Mountains, Iran, and Rocky Mountains, Canada. University of Waterloo. MSc Thesis.
Roberts, N.J., Evans, S.G., 2013. The gigantic Seymareh (Saidmarreh) rock avalanche, Zagros Fold-Thrust Belt, Iran. J. Geol. Soc. 170, 685–700.
Rouhi, J., Delchiero, M., Della Seta, M., Martino, S., 2022. New insights on the emplacement kinematics of the Seymareh landslides (Zagros Mts., Iran) through a novel spatial statistical approach. Frontiers. Earth Sci. 10, 869391.
Roustaei, M., Nissen, E., Abbassi, M., Gholamzadeh, A., Ghorashi, M., Tatar, M., Yamini-Fard, F., Bergman, E., Jackson, J., Parsons, B., 2010. The 2006 Marc 25 Fin earthquakes (Iran)-insights into the vertical extents of faulting in the Zagros simply Folded Belt. Geophys. J. Int. 181, 1275–1291.
Scheidegger, A.E., 1973. On the prediction of the reach and velocity of catastrophic landslides. Rock Mech. 5, 231–236.
Sepehr, M., Cosgrove, J.W., 2004. Structural framework of the Zagros fold–thrust belt, Iran. Mar. Petrol. Geol. 21, 829–843.
Sharafi, S., Yamani, M., Ehteshami-Moinabadi, M., 2019. Evidence of the formation of landslide-dammed lakes in the Zagros Mountains range, Iran. J. Mt. Sci. 16, 2389–2403.
Sherkati, S., Molinaro, M., de Lamotte, D.F., Letouzey, J., 2005. Detachment folding in the Central and Eastern Zagros fold-belt (Iran): salt mobility, multiple detachments and late basement control. J. Struct. Geol. 27, 1680–1696.
Sherkati, S., Letouzey, J., Frizon de Lamotte, D., 2006. Central Zagros fold-thrust belt (Iran): New insights from seismic data, field observation, and sandbox modeling. Tectonics 25, TC4007.
Shoaei, Z., 2014. Mechanism of the giant Seimareh Landslide, Iran, and the longevity of its landslide dams. Environ. Earth Sci. 72, 2411–2422.
Shreve, R.L., 1968. The Blackhawk Landslide, 108. Geological Society of America special paper.
Stephenson, B.J., Koopman, A., Hillgartner, H., McQuillan, H., Bourne, S., Noad, J.J., Rawnsley, K., 2007. Structural and stratigraphic controls on fold-related fracturing in the Zagros Mountains, Iran: implications for reservoir development. Geol. Soc. Lond., Spec. Publ. 270, 1–21.

Stöklin, J., 1968. Structural history and tectonics of Iran: a review. Am. Assoc. Pet. Geol. Bull. 52, 1229–1258.
Strom, A., 2015. Clustering of large bedrock landslides and recurrent slope failure: implications for land seismic hazard assessment of the Tien Shan-Djungaria region. Int. J.Geohazards Environ. 1, 110–121.
Strom, A., Li, L., Lan, H., 2019. Rock avalanche mobility: optimal characterization and the effects of confinement. Landslides 16, 1437–1452.
Talbot, C.J., Alavi, M., 1996. The past of a future syntaxis across the Zagros. Geol. Soc. Lond., Spec. Publ. 100, 89–109.
Talebian, M., Jackson, J., 2004. A reappraisal of earthquake focal mechanisms and active shortening in the Zagros mountains of Iran. Geophys. J. Int. 156, 506–526.
Tavakoli, F., Walpersdorf, A., Authemayou, C., Nankali, H.R., Hatzfeld, D., Tatar, M., Djamour, Y., Nilforoushan, F., Cotte, N., 2008. Distribution of the right-lateral strike–slip motion from the Main recent Fault to the Kazerun Fault System (Zagros, Iran): evidence from present-day GPS velocities. Earth Planet. Sci. Lett. 275, 342–347.
Vernant, P., Nilforoushan, F., Hatzfeld, D., Abbassi, M.R., Vigny, C., Masson, F., Nankali, H., Martinod, J., Ashtiani, A., Bayer, R., Tavakoli, F., Chéry, J., 2004. Present-day crustal deformation and plate kinematics in the Middle East constrained by GPS measurements in Iran and northern Oman. Geophys. J. Int. 157, 381–398.
Vergés, J., Emami, H., Garcés, M., Beamud, E., Homke, S., Skott, P., 2019. Zagros foreland fold belt timing across Lurestan to constrain Arabia-Iran collision. In: Saein, A.F. (Ed.), Developments in Structural Geology and Tectonics, Vol. 3. Elsevier, Amsterdam, pp. 29–52.
von Poschinger, A., Kippel, Th., 2009. Alluvial deposits liquefied by the Flims rock slide. Geomorphology 103, 50–56.
Walker, R.T., Andalibi, M.J., Gheitanchi, M.R., Jackson, J.A., Karegar, S., Priestley, K., 2005. Seismological and field observations from the 1990 November 6 Furg (Hormozgan) earthquake: a rare case of surface rupture in the Zagros mountains of Iran. Geophys. J. Int. 163, 567–579.
Walker, R.T., Khatib, M.M., Bahroudi, A., Rodés, A., Schnabel, C., Fattahi, M., Talebian, M., Bergman, E., 2015. Co-seismic, geomorphic, and geologic fold growth associated with the 1978 Tabas-e-Golshan earthquake fault in eastern Iran. Geomorphology 237, 98–118.
Walpersdorf, A., Hatzfeld, D., Nankali, H., Tavakoli, F., Nilforoushan, F., Tatar, M., Vernant, P., Chéry, J., Masson, F., 2006. Difference in the GPS deformation pattern of North and Central Zagros (Iran). Geophys. J. Int. 167, 1077–1088.
Wang, H.B., Sassa, K., Xu, W.Y., 2007. Analysis of a spatial distribution of landslides triggered by the 2004 Chuetsu earthquakes of Niigata Prefecture, Japan. Nat. Hazards 41, 43–60.
Wells, D.L., Coppersmith, K.J., 1994. New empirical relationships among magnitude, rupture length, rupture width, rupture area, and surface displacement. Bull. Seismol. Soc. Am. 84, 974–1002.
Wessel, B., 2016. TanDEM-X Ground Segment – DEM Products Specification Document. EOC, DLR, Oberpfaffenhofen, Germany, Public Document TD-GS-PS-0021, Issue 3.2, 2016. Available: https://tandemx-science.dlr.de/.